Thermoelastic Modeling of the CubeSat Laser Infrared CrosslinK (CLICK) Payloads

by

William John Kammerer III

B.S., University of Massachusetts Lowell, 2018

Submitted to the Department of Aeronautics and Astronautics
in partial fulfillment of the requirements for the degree of

Master of Science in Aeronautics and Astronautics

at the

MASSACHUSETTS INSTITUTE OF TECHNOLOGY

September 2020

Author .....
Department of Aeronautics and Astronautics
August 18th, 2020

Certified by .....
Kerri Cahoy
Associate Professor of Aeronautics and Astronautics
Thesis Supervisor

Accepted by .....
Zoltan Spakovszky
Professor of Aeronautics and Astronautics
Chair, Graduate Program Committee

This page was left intentionally blank.

Thermoelastic Modeling of the CubeSat Laser Infrared CrosslinK (CLICK) Payloads

by

William John Kammerer III

Submitted to the Department of Aeronautics and Astronautics
on August 18th, 2020, in partial fulfillment of the
requirements for the degree of
Master of Science in Aeronautics and Astronautics

Abstract

Radio frequency (RF) communication is the typical way that small satellites transmit data from space to the ground. Laser communication (lasercom) can provide lower size, weight, and power (SWaP) compared with RF communication systems. The CubeSat Laser Infrared CrosslinK (CLICK) mission is a series of three 3U CubeSats with low SWaP lasercom payloads. The mission has two phases: CLICK-A, which is downlink lasercom only, and CLICK-B/C, which will perform both crosslink and downlink lasercom experiments. CLICK-A will provide a 10 Mbps downlink data rate to a 28 cm aperture portable optical ground station. CLICK-B/C will provide at least 20 Mbps crosslink at ranges from 25 km to 580 km and with ranging capability better than 50 cm (optical time precision of 1.6 ns). This thesis focuses on the engineering analysis that has gone into the thermal design of the CLICK lasercom payloads. We first provide an overview of the mechanical design, electrical power consumption, and the concept of operations for each of the payloads, which is used to predict on orbit temperatures. The CLICK-A payload thermal model is described and the results of the model are shown. We also describe thermal vacuum testing of a camera and lens that are used both for the CLICK-A and CLICK-B/C payloads. The CLICK-B/C payloads thermal model is described and the results of the model are shown. Thermoelastic analysis is performed to determine the pointing error induced by the shifting of optics within the CLICK-B/C payloads. The thermal models predict all components will stay within survival temperatures, and that all components will be able to be preheated to within their operational temperature bounds. This work contributes to the development of CLICK payloads and the state of the art for miniaturized free space optical communication technologies.

Thesis Supervisor: Kerri Cahoy
Title: Associate Professor of Aeronautics and Astronautics

This page was left intentionally blank.

Acknowledgments

It is hard to put into words what the last two years have meant to me. Never in my wildest dreams did I believe that I could be as fortunate to study with such a passionate and interesting group of people as those who I have met during my time at MIT. This has been a journey that I could not have made if it were not for many individuals who have pushed, guided, and enabled me to be where I am today.

First, I would like to thank my graduate advisor Kerri Cahoy. Every now and again there are people who you meet and they radically change your perspective on life. Kerri Cahoy is one of those people. She took me on as a student and gave me a home in STAR lab to flourish. She has demonstrated to me, and the people she leads, how selfless a person can be. She has shown me that people are capable of so much, if they believe in what they are doing. She has pushed me to expand beyond my comfortable area of knowledge and provided support whenever I needed it. The past two years in graduate school have provided me a level of experience in the design, building, and testing of CubeSat payloads that I could have only dreamed of. The lab Kerri has built is a community of people who are passionate about space exploration and using space to help expand our understanding of the universe around us. The help and guidance she has given me, and the people around her, is hard to truly put into words, but I know that I will forever be changed by her example as an advisor and leader that I was fortunate enough to work under.

I would also like to thank my girlfriend Valerie. She has been not only an emotional bedrock for me, but also a great friend. She has helped me through many difficult phases of life, especially the past two years of graduate school, more than I could ever fully express. I would not be the person I am today if she was not there to help keep me on the right track. Special thanks for putting up with all the ridiculous hours I would pull during classes and supporting me. I look forward to all the adventures we will share together.

I must thank the CLICK project for providing a phenomenal project to cut my teeth on as a young engineer. It has been a thrill to learn how optical communication

works and to be part of the team helping to advance this technology.

I would also like to thank my family. They have helped me realize there is more to life than what you do for a job. When times got tough, they were there to listen to me and nod in excitement as I spout off how cool space is.

I must also thank from the bottom of my heart Linda Fuhrman, for if it were not her amazing mentoring and guiding me through the graduate school application process, I would not be as lucky to have experienced the last two years. Linda helped me believe in myself before I even thought I could. There is nothing I could say or do to try to repay what she did to encourage and enable in me. I can only hope that I can mentor future young engineers as well as she mentored me.

Lastly, I would like to thank my high school physics teacher, TJ Noviello. He began me on this journey of unlocking the potential I had in me by pushing and showing me you can do things you previously thought impossible. His tireless dedication to the many students he has taught is an example of what an educator should strive to achieve.

Contents

List of Figures

List of Tables

This page was left intentionally blank.

Chapter 1

Introduction

CubeSats create opportunities for universities and companies to test space payloads with lower cost access to space. CubeSat data collection capabilities has been advancing and this data needs to be transmitted to the ground [1]. When the ability of a satellite to generate data is greater than the downlink capability, the data must be compressed or a limited set of data must be downlinked, as done recently for missions such as the Hyperspectral Thermal Imager (HYTI) mission [2]. There have been advances in both radio frequency (RF) and optical communication systems for CubeSats. On the RF technology side, companies have been able to achieve high data rates for CubeSats, up to 1.6 Gbps with X-band transmitters, but these radios are not yet available commercially [3]. This work focuses on optical communication, which can to improve the data transfer capabilities of CubeSats by several orders of magnitude [4]. The work presented in this thesis advances technology in optical downlink from space to Earth, as well as optical intersatellite data transfer corsslinks.

1.1 CubeSats

The CubeSat standard was developed by two professors, Bob Twiggs of Stanford University and Jordi Puig-Suari of California Polytechnic State University, as a tool for students to gain hands-on experience in the design, building, and testing of space systems hardware [5]. The format of a CubeSat is defined by the U, with one U being

10 cm by 10 cm by 10 cm. Currently, there are standards for 1U, 2U, 3U, and 6U CubeSats, but other larger sizes, such as 12U and 16U do not have a standard. The CubeSat Program at California Polytechnic State University publishes the CubeSat Design Specification, which the industry uses in the design of components for these satellites. The design specification for a 3U CubeSat is shown in Figure 1-1 [6].

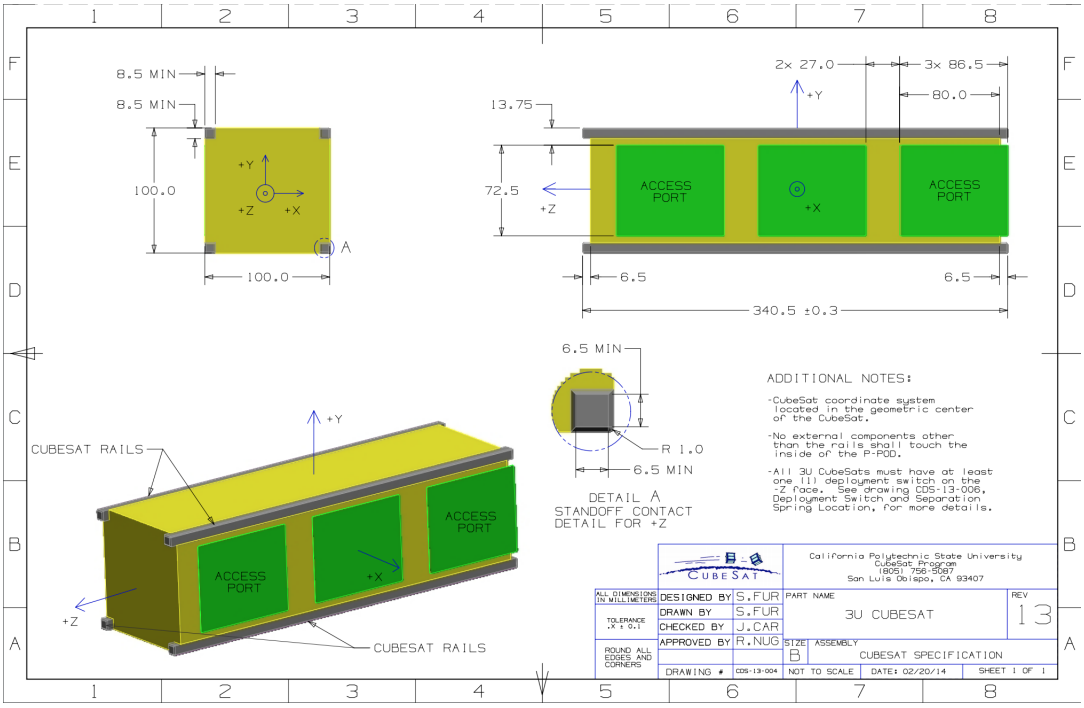

Figure 1-1: 3U CubeSat design specification [6].

The popularity of CubeSats has been steadily growing as shown in Figure 1-2 [7]. CubeSats of all sizes have been built for a variety of purposes. They started out as an educational tool, but have expanded into a platform for researchers and companies to demonstrate feasibility of novel technology in space. The industry has seen the emergence of companies providing commercial off-the-shelf (COTS) components and spacecraft buses for CubeSats.

Examples of missions that have validated the CubeSat platform and contributed to research in the scientific community include:

1. ASTERIA, 6U CubeSat that was launched and deployed in 2017. It demonstrated transient exoplanet detection through the use of a temperature controlled focal plane and a two-stage pointing system [8].

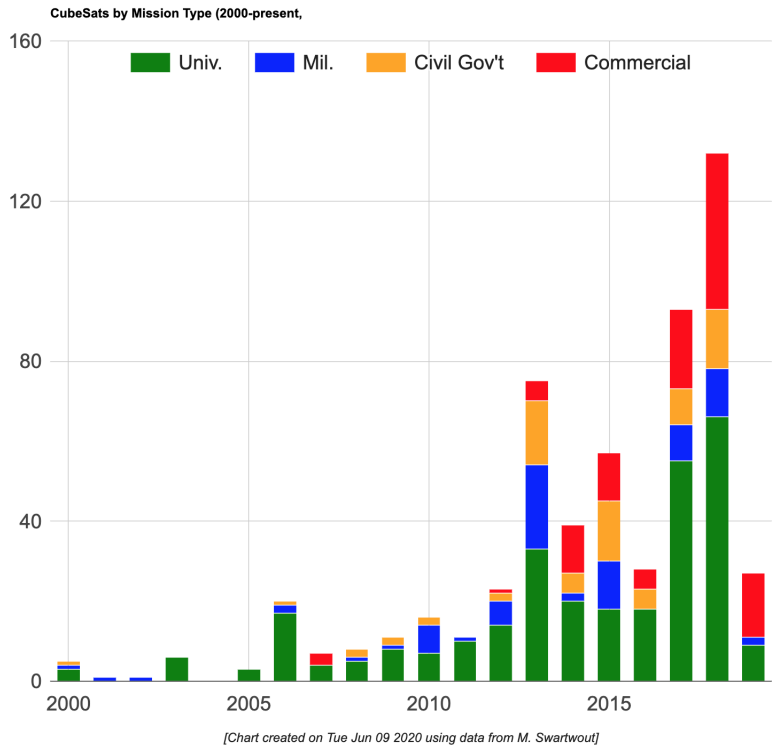

Figure 1-2: Number of CubeSats launched per year [7].

2. The MarCO CubeSats, a pair of identical 6U CubeSats that were the first interplanetary CubeSats, used as a radio relay for the landing of the Insight Mars lander in November 2018. The two CubeSats were able to relay over 90% of the telemetry from Insight in real time as it was landing, which would not have been possible without the CubeSats [9].

3. The MicroMAS-2A and TEMPEST-D missions demonstrated atmospheric temperature and humidity sounding through the use of onboard scanning microwave radiometers [10][11].

1.2 Optical Communication

Optical communication is the use of visible and infrared energy to transmit information [12] and is often referred to laser communications (lasercom). Communication using optical fibers has been transformative for distributing large volumes of information rapidly; much of the backbone internet infrastructure utilizes such technology.

For communication from space, the optical signal is transmitted through a free-space channel. Space links can be downlink (space to ground), uplink (ground to space), or crosslink (space to space).

When comparing optical communication to traditional RF communication, optical has a few advantages. First, optical communication has shorter wavelengths, and therefore lower beam divergence compared to RF [13]. The beam divergence is a characterization of how much the transmitted power spreads as a function of distance. The beam divergence of a transmitted signal is proportional to wavelength divided by the diameter of the transmitter [14]. Optical wavelengths therefore have an advantage over radio wavelengths due the smaller wavelength. A narrower beam divergence results in an increase in power at the receiver over a given distance. While this is advantageous, it also leads to an increase in the pointing requirements of the system [15]. A second advantage is the inherit security due to the narrow beam divergence, this means that it is harder to try to intercept an optical communication signal. The receiver attempting to intercept the signal must be within the area of the beam divergence cone when it is trying to receive, but since the beam width is smaller with a narrower beam divergence for a given distance, the area for trying to intercept a signal is dramatically reduced compared to RF communications. A third advantage is that there is currently no regulatory license needed for transmitting since optical wavelengths are currently unregulated. RF systems require a license to broadcast to and from space. Small satellite programs sometimes struggle to get licenses to use part of the RF spectrum through the Federal Communications Commission or International Telecommunication Union [4]. Another advantage is that the size, weight, and power (SWaP) of an optical transmitter can be smaller compared to an RF system [15].

There are also inherent disadvantages to optical communications. One is that downlinks have the problem of atmospheric attenuation and the inability to penetrate cloud cover [15]. The atmospheric attenuation is a non-deterministic factor when trying to determine the required power of the transmitter to get a certain margin with a link budget [15]. The inability to penetrate cloud cover complicates the operations

of a communication system as well, although networks with crosslinks have been proposed to help make a system feasible.

There have been a series of optical communication demonstrations in space. A selection of missions is shown in Table 1.1 [16] [17]. Of the missions shown in Table 1.1, the only CubeSat was OCSD. OCSD stands for Optical Communications and Sensors Demonstration, a pair of 1.5U CubeSats that used body pointing and on-off keying (OOK) modulation to achieve a 200 Mbps data rate. OCSD was the first CubeSat to demonstrate optical communications. Another notable mission is Aerocube-11 (also called R3), a pair of 3U CubeSats designed to provide multispectral imaging of Earth, with a laser downlink that is operationally the same as OCSD [18]. Also designed by the Aerospace Corporation, the R3 CubeSats lasercom performance was similar to OCSD. The R3 CubeSats reported to have achieved 100 Mbps downlink, which was critical in downlinking the large volume of data generated by the CubeSats [**?**].

Table 1.1: Selected subset of free space optical communication missions [16] [17].

Year	**Mission**	**Organization**	**Link Type**	**Data Rate (Gbps)**
2001	GeoLITE ALEX	MIT Lincoln Laboratory	GEO-Ground GEO-Air	>1
2001	SILEX	ESA	LEO-GEO	0.05
2005	LUCE	JAXA	LEO-GEO LEO-Ground	0.05
2008	NFIRE/ TerraSAR-X	Tesat Spacecom	LEO-LEO LEO-Ground	5.65
2013	LLCD	MIT Lincoln Laboratory/NASA	Moon-Ground	0.622
2014	OPALS	JPL	ISS-Ground	0.05
2014	EDRS	Tesat Spacecom/ ESA	LEO-GEO GEO-ground	1.8
2017	OCSD	Aerospace Corporation	LEO-Ground	0.2

1.3 CLICK Mission

The CubeSat Laser Infrared CrosslinK (CLICK) mission began in 2018 as the combination of separate efforts within two university projects. The Space Telecommunications, Astronomy, and Radiation (STAR) Lab at Massachusetts Institute of Technology (MIT) had designed and prototyped a downlink payload, called the Nanosatellite Optical Downlink Experiment (NODE), as well as developed a crosslink project called the Free-space Lasercom And Radiation Experiment (FLARE). The MIT projects combined with the optical time transfer work being done at the Precision Space Systems Laboratory (PSSL) at the University of Florida (UF) [19], to create the CLICK mission. CLICK is jointly developed the MIT, UF, and the NASA Ames Research Center. The project will advance the state of the art for miniaturized free space optical communication technologies by including MEMS fast steering mirrors (FSM) to augment spacecraft body steering and a chip scale atomic clock (CSAC) for optical time transfer. The CLICK-A and CLICK-B/C payloads being developed are equipped with infrared lasers that use pulse position modulation (PPM). The mission plan includes two phases that involves two separate launches, CLICK-A and CLICK-B/C, for a total of three 3U CubeSats. An outline of the mission phases and their payloads is shown in Figure 1-3 [20]. The project is funded through through the Space Technology Mission Directorate (STMD) at NASA.

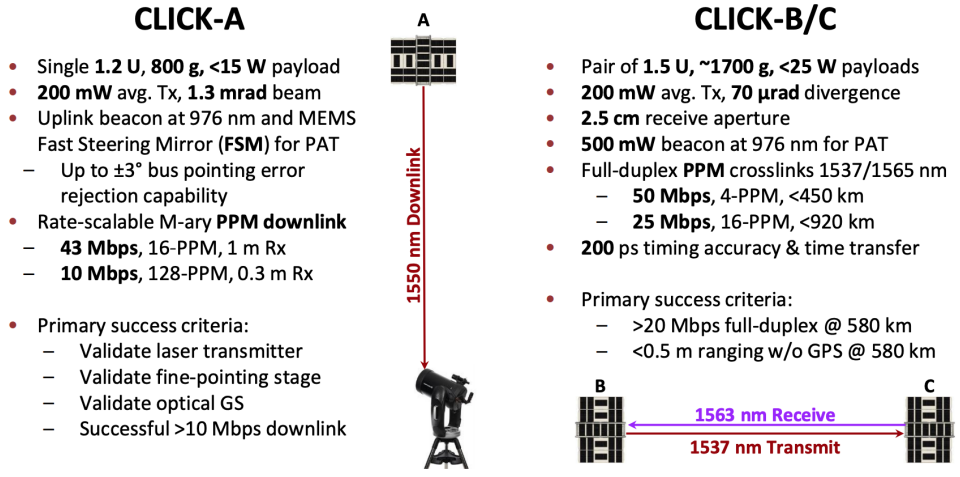

Figure 1-3: Summary of CLICK mission phases [20].

1.3.1 CLICK-A Payload

The CLICK-A payload is designed to demonstrate optical communication downlink, at a rate of 10 Mbps, to a 28 cm astronomy telescope equipped with electronics to receive signals, that serves as an optical ground station [21]. The CLICK-A demonstration also serves as a risk reduction for the CLICK-B/C demonstration. The primary purpose is demonstrating use of MEMS FSM for fine pointing, which will be used for downlink on CLICK-A and crosslink on CLICK-B/C. The CubeSats have similar spacecraft buses, steering mirrors, optical amplifiers, beacon tracking cameras and lenses. The CLICK-A payload is shown in Figure 1-4.

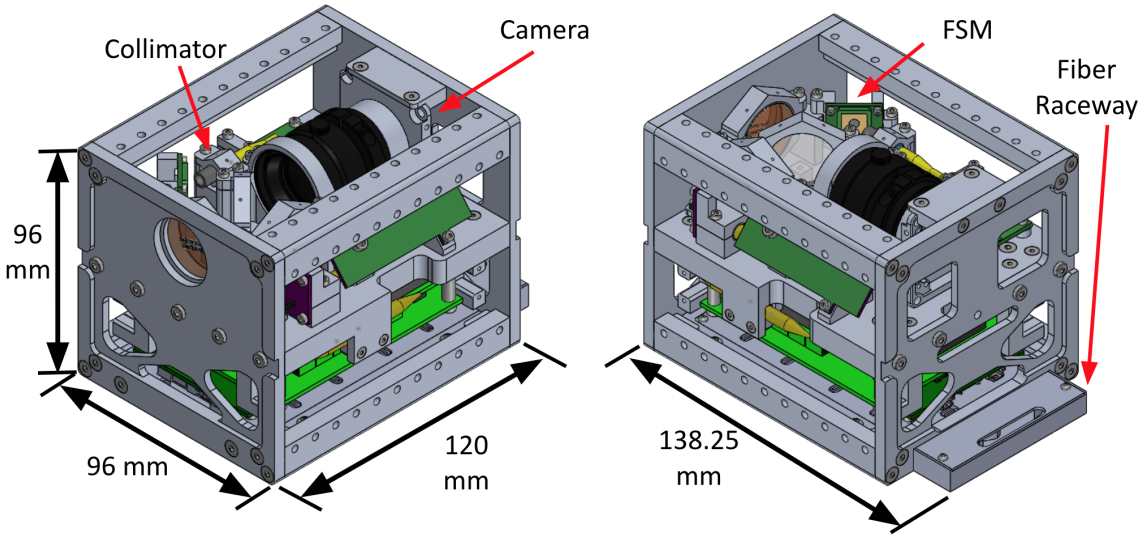

Figure 1-4: CLICK-A payload mechanical design from CLICK-A CAD V1.4 model.

The CLICK-A downlink payload is roughly 1.2U. There is an additional fiber raceway that extends the payload's length to 138.25 mm. The CLICK-A payload current best estimate mass is 1300 grams. The CLICK-A mechanical design includes an optical bench, which sits in the middle of the payload and is used as part of the structure. The optical bench is used to mount the free space optical components. Underneath to optical bench is where most of the electronics that control the payload are located, as well as the optical amplifier. The optical bench is supported by the front and back plates. These plates also serve as mounting locations for the rails that run along the corners of the payload. The rails are the components used to interface

with and attach to the Blue Canyon Technologies XB3 spacecraft bus that hosts the CLICK-A payload.

The payload operates at a wavelength of 1550 nm. The modulation of the light is performed by controlling the wavelength of the seed laser to be in-band and out-of-band of a fiber Bragg grating (FBG). When the wavelength of the seed laser is matched to the FBG in-band wavelength, the light that is fed into the FBG is reflected back down the input fiber. This approach, paired with an optical circulator which only lets light travel in one direction, allows the in-band light to pass through the circulator. Small changes in the seed laser wavelength can move the light out-of-band again, making the optical pulse [22]. A diagram of how these components interface is shown in Figure 1-5 [22]. The modulated light is then fed into an Erbium-doped fiber amplifier (EDFA) which is able to amplify the power of the light to around 200 mW.

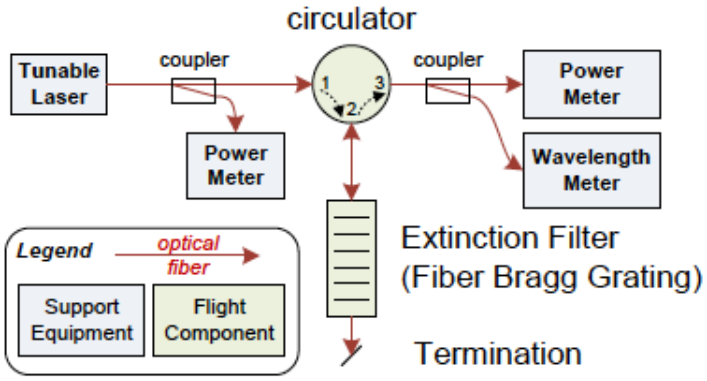

Figure 1-5: Diagram of modulation setup using a FBG and a circulator. Picture from Ryan Kingbury's PhD thesis. [22].

The CLICK-A payload is designed with a fine pointing system built-in to be able to provide better pointing capabilities of the transmitted light than what the spacecraft bus offers. The optical layout is shown in Figure 1-6, alongside the mechanical layout of the payload. The modulated light in the optical fibers at 1550 nm is combined with a calibration laser that operates at 635 nm. The combined light leaves the optical fiber and is fed into a collimator, which then reflects off a fast steering mirror (FSM). The FSM is used to control the angle of the collimated light as it leaves the payload.

The FSM reflects light onto a dichroic beam splitter (DBS). The DBS reflects 99.7% of the 1550 nm modulated light but passes 50% of the 635 nm calibration light. The reflected 1550 nm light then passes through a double bandpass filter designed to pass only 1550 nm and 976 nm light. The 635 nm light that is passed through the DBS is then reflected off of a mirror back onto the DBS. The DBS passes 50% of this light and 50% is reflected into a lens which focuses the 635 nm light on to the focal plane array (FPA) of the beacon camera. This light is used to calibrate and control the FSM. As it transmits, the spacecraft is roughly pointing the payload at where it thinks the ground station is located. The ground station is equipped with a 976 nm laser that acts as an uplink beacon to help the spacecraft find and point to the ground station. The 976 nm light from the ground beacon passes through the double bandpass filter and the DBS into the lens which focuses it onto the FPA of the camera. When the camera sees both the spot of light from the beacon and the spot of light from calibration laser internally, it aligns those spots to ensure the light is being pointed in the right direction [23].

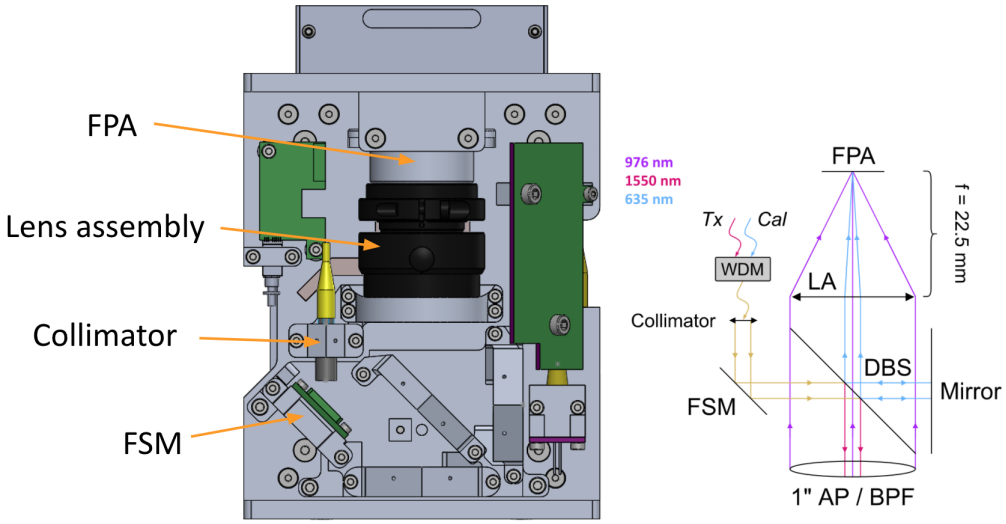

Figure 1-6: Top down view of CLICK-A mechanical design (left) compared to top down view optical layout (right) [23]. Mechanical desgn picture from CLICK-A CAD V1.4 model.[23].

The payload is designed to be integrated into a host spacecraft that provides the course pointing of the payload as well as power and a traditional RF communica-

tions link to the ground. A bus procurement process was performed by NASA Ames Research Center for this mission, and Blue Canyon Technologies was awarded the contract to supply one XB3 spacecraft for the CLICK-A payload and two XB3 spacecraft for the CLICK -B and -C payloads. The thermal aspects of the payload/bus interface are a key focus on the thermal model in this thesis and discussed in Chapter 3. The mechanical, thermal, power, and data interfaces are defined in the payload-to-bus interface control document A9SP-1803-XR003 Rev. G.

Once the CubeSat is in orbit, the CLICK-A payload will attempt to communicate to a portable optical ground station made from an astronomy telescope. The telescope is a Celestron CPC 1100, and provides a 28 cm aperture for receiving the light from the payload. The ground station is called the Portable Telescope for Lasercom (PorTeL). The light coming into the optical telescope is focused on a avalanche photodiode sensor board that is attached to an oscilloscope to record the light pulses received on the sensor. The development and operation of the PorTeL system was the topic of Kathleen Riesling's PhD thesis [24]. The PorTeL optical ground station has been continually improved by our team, and a team at ESA has made their own version of the project as well. Figure 1-7 shows what PorTeL looks like.

Figure 1-7: Portable optical telescope (PorTeL) used for CLICK mission [24].

The CLICK-A mission already has a launch and deployment scheduled through the

CubeSat Student Launch Initiative (CSLI). The mission will be soft-stowed as Cargo on a International Space Station (ISS) resupply mission. Once in space, the CubeSat will be deployed by NanoRacks. After deployment, a timer starts for 45 minutes, after which the spacecraft will turn on and deploy solar panels. Once operating, spacecraft will go through a commissioning phase to establish contact and confirm nominal operation of the spacecraft and payload. Once commissioned, the spacecraft will can begin testing optical downlink testing to PorTeL. The overall concept of operations for CLICK-A is shown in Figure 1-8.

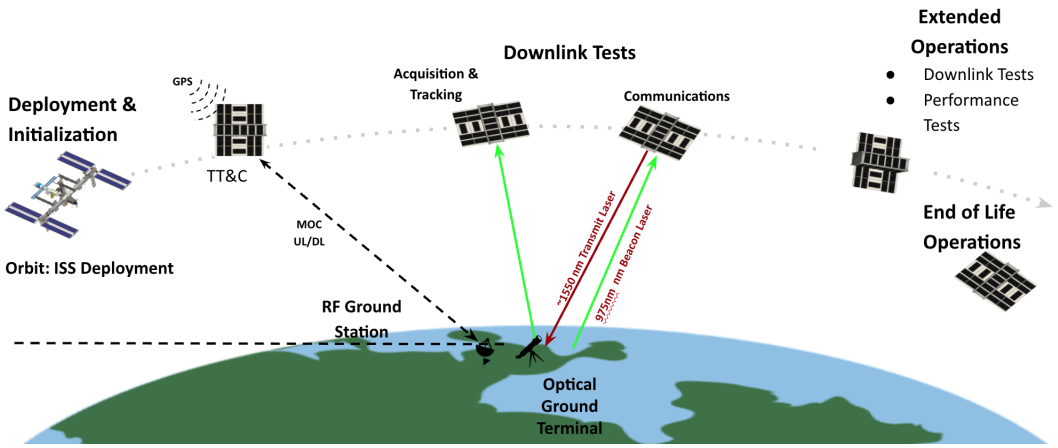

Figure 1-8: CLICK-A concept of operations. Source: CLICK-A design review with NASA Ames.

1.3.2 CLICK-B/C Payloads

The CLICK-B and -C CubeSats are designed to demonstrate optical communication crosslinks to eachother as well as downlinks to PorTeL. The two payloads are designed to achieve crosslink communications rates of at least 20 Mbps at ranges from 25 km to 580 km. Each payload also has a chip scale atomic clock (CSAC) for optical time transfer enabling a ranging capability of better than 50 cm (1.6 ns) [25]. The two payloads are nearly identical with the only difference being the wavelength they transmit and receive at. The CAD model of the CLICK- B/C payload is shown in Figure 1-9.

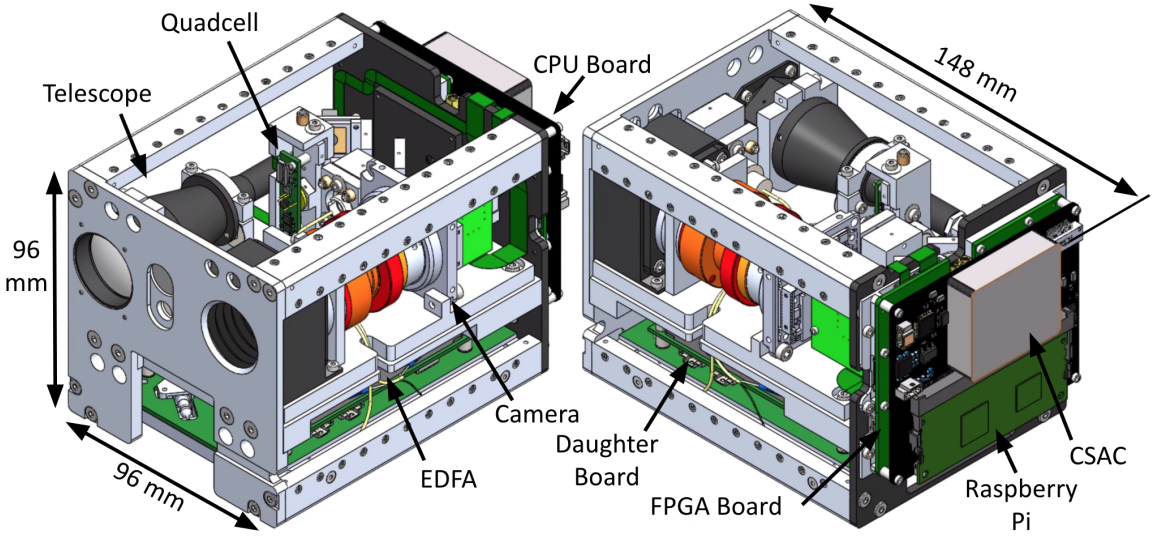

Figure 1-9: CLICK-B/C payload from V1.4 CAD model.

The CLICK-B/C payload is about 1.5U. The payload current best estimate mass is around 1700 grams. The CLICK-B/C payload differs in mechanical design from the CLICK-A payload in its approach to mounting optics. The CLICK-B/C payload uses a dedicated optical bench for mounting all the optics of the design, unlike CLICK-A where the optical bench also serves as the main structure. The dedicated optical bench was pursued for two reasons. First, it is easier to align the optics on the optical bench when the optical bench can be removed from the structure of the payload. Second, thermal isolation of the optical bench to helps to reduce thermoelastic shifts. The rest of the mechanical design is fairly similar to CLICK-A with electronics sitting below the plate that mounts the optical bench. The optical amplifier and electronics are mounted underneath this plate. There are front and back plates that mount the middle plate. The front and back plates also serve as mounting locations for the rails that run along the corners of the payload. The rails are very similar to the CLICK-A design and are used to interface with and attach to the spacecraft bus that hosts each CLICK-B/C payload. Another difference from CLICK-A is the addition of electronic boards at the rear of the payload. Mounted between the back plate and the FPGA board is a heat spreader that is designed to sink the heat from the FPGA board into the back plate of the payload.

The CLICK-B/C payloads operate at two different wavelengths to enable full

duplex crosslinks. The CLICK-B payload transmits at 1537 nm and the CLICK-C payload transmits at 1563 nm. The reason for the two wavelengths has to do with full duplex operation and the payload receive filters. If the payload was both transmitting and receiving at 1550 nm, then it would self-contaminate, and likely detect the light it produced. This becomes an issue when trying to receive from the other payload, which would also transmit at 1550 nm; the receiving payload would be unable to distinguish the light it transmitted from the light it received from the other payload. To prevent this, each payload operates at 13 nm away from the central frequency of 1550 nm. With the appropriate filters and laser sources, the CLICK-B payload transmits at 1537 nm and receives at 1563 nm, while the CLICK-C payload transmits at 1563 nm and receives at 1537 nm. The modulation of this light is currently being modified from the initial plan. Originally, the plan was to use the same laser and FBG set up as CLICK-A, but it was discovered that the company Broadcom was no longer producing the 1611F050 and 1611F017 lasers needed. Due to this procurement challenge, the modulating architecture of the payload is currently being updated to work with available components. CLICK-B/C shares the same Erbium-doped fiber amplifier (EDFA) as CLICK-A. The expected optical power after the EDFA is around 200 mW.

The optical layout of the CLICK-B/C is more complex than CLICK-A and is shown in Figure 1-10. A labeled version of the CLICK-B/C optical bench CAD is shown in Figure 1-11. A ray trace of how the light behaves through the optical train is overlaid on top of the CLICK-B/C optical bench CAD in Figure 1-12. In CLICK-A, there is a 976 nm uplink beacon that is transmitted from the PorTeL optical ground station, which is used to coordinate pointing the payload. For the CLICK-B/C payloads, the payloads each have their own 976 nm beacon for the other payload to be able to point precisely at each other. The beacon laser beam divergence is much larger compared to the laser used for communication. The larger beam divergence means that it is easier for the payload to see and therefore easier to close coarse pointing acquisition. The payloads have the same cameras and lenses that are being used for the CLICK-A mission for the coarse acquisition of the beacon. Since the field

of view of the camera and lens is large, the payload is able to tell the spacecraft how to adjust its pointing to be pointed at the other payload based on what this beacon camera is sensing.

Once the coarse acquisition is closed, the next train of optics is utilized. The transmitting and receiving part of the optics starts with a telescope that has a one inch aperture. The first lens (L1) of the telescope focuses the light down just past a pinhole built into the telescope. There is another optic (L2) that is used to focus the light leaving the telescope onto the quadrature photodiode (quadcell). This sensor is used to determine the position of the beacon light spot. After the light leaves L2, the light reflects off a FSM that is used to do the fine pointing of the payload, similar to the pointing system of CLICK-A. After reflecting off the FSM, the 976 nm light received through the telescope then reflects off a filter designed to reflect the 976 nm wavelength of the beacon and pass the crosslink ∼1550 nm wavelength of the other payload. The 976 nm beacon light then hits the quadrature photodiode to determine how the FSM is influencing the light reflecting off it. The crosslink ∼1550 nm light that is passed through the first filter then hits a second filter that is designed to pass the received crosslink light from the other payload, while reflecting the current payload's transmitted light. Once the received crosslink ∼1550 nm light passes through the second filter, it is hits another lens (L3), which focuses the light onto an avalanche photodiode (APD). The APD is used to sense the received signal and fed into electronics to be demodulated. The transmitted light from the payload leaves the fiber from the transmit collimator (Tx) and is reflected off the second filter. That transmitted light then passes back through the optical train to outside the payload.

Just as with the CLICK-A payload, the CLICK-B/C payloads are each hosted by a Blue Canyon Technologies XB3 spacecraft bus. This bus provides the coarse pointing of the payload as well as power and a traditional RF communications link to the ground for command and control. It also provides as RF communications crosslink to coordinate optical transmission experiments between the two satellites. The interface between the CLICK-B/C payload and the spacecraft is almost identical

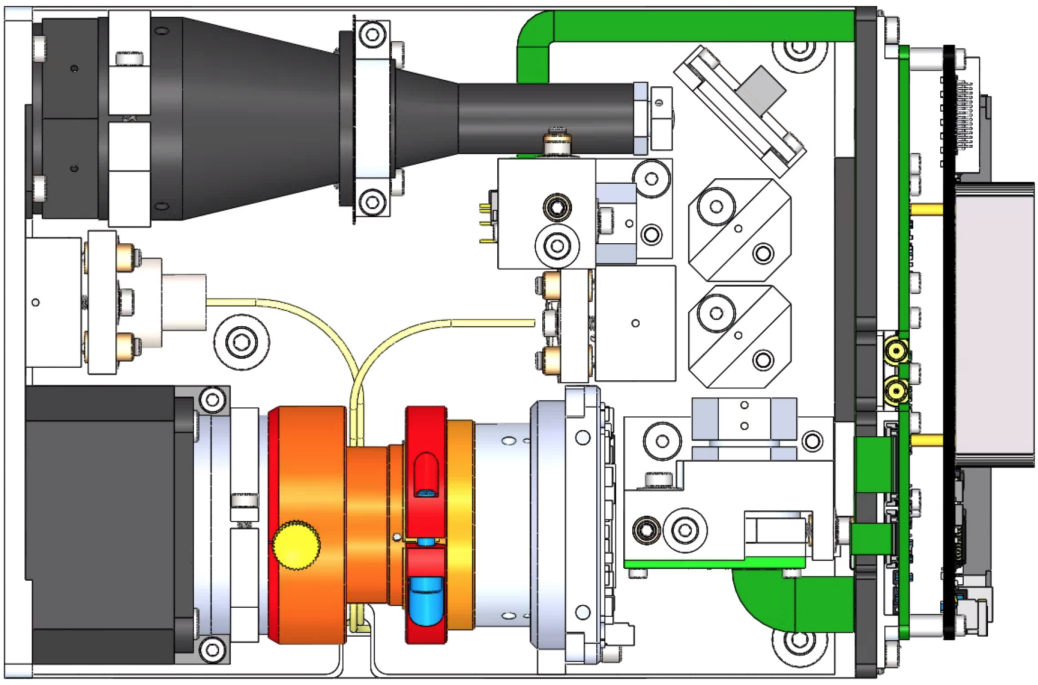

Figure 1-10: CLICK-B/C optical bench mechanical design from CAD model V1.4.

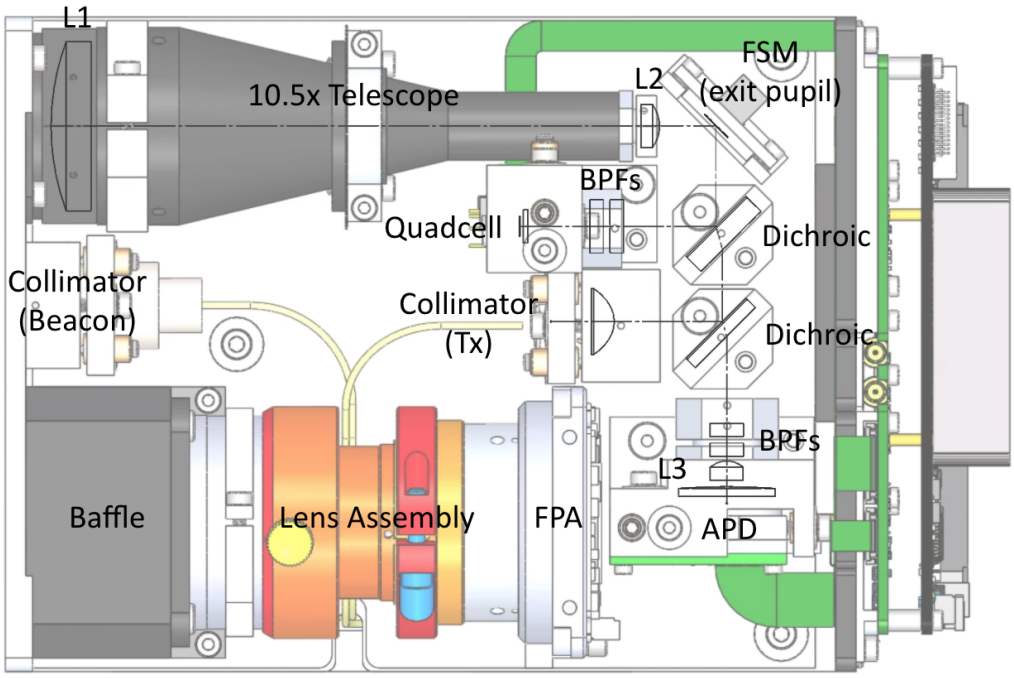

Figure 1-11: CLICK-B/C optical bench mechanical design with labeled component layout from CAD model V1.4. Source: Peter Grenfell

to CLICK-A, and the thermal aspects of this will be elaborated on in chapter 3.

The CLICK-B/C mission has also been selected to launch as part of the CubeSat

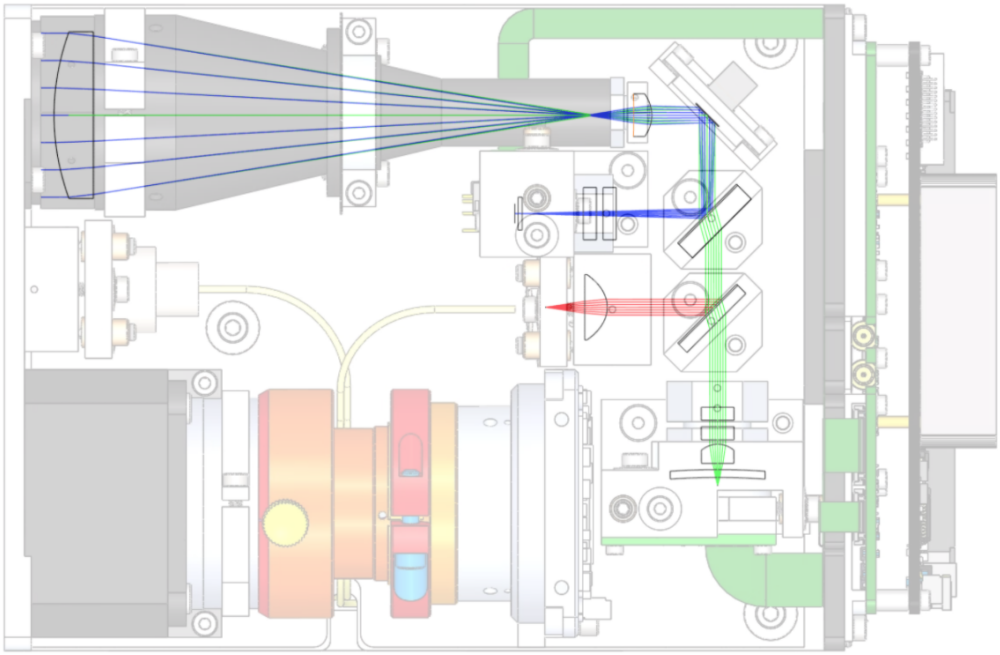

Figure 1-12: CLICK-B/C optical ray tracing. Blue is the 976 nm light. Green is the received transmission wavelength. Red is the broadcasting transmission wavelength. Source: Peter Grenfell and Ondrej Čierny.

Student Launch Initiative (CSLI), but the exact rocket and orbit that the spacecraft will be placed into has yet to be determined. It is expected that the CubeSats will be deployed into space through typical CubeSat deployers. After deployment, a timer starts for 45 minutes to then turn on the spacecraft and deploy solar panels. Once operating, the spacecraft will be in a safe mode until the payload is commissioned. Once CLICK-B/C are in orbit, the payloads will be configured into a differential drag configuration [25]. This changes which face of the satellite will be oriented toward the velocity vector of the spacecraft. Orienting a larger area face in the direction of velocity causes more drag on the satellite compared to a face with a smaller area. Setting one satellite to an orientation with a higher drag and one into a lower drag allows a separation to form relative to each other. This is critical to ensure that the proper link distances, 25 km to 580 km, are established to test the crosslink capability of the payloads. Once at the chosen separation, the payloads will attempt with communicate to each other. First, an RF crosslink is established to trade ephemeris data, then an optical crosslink is attempted. Each of these payload is also able to

communicate to a portable optical ground station, PorTeL, that was described in the previous section. The overall concept of operations of the satellite is shown in Figure 1-13.

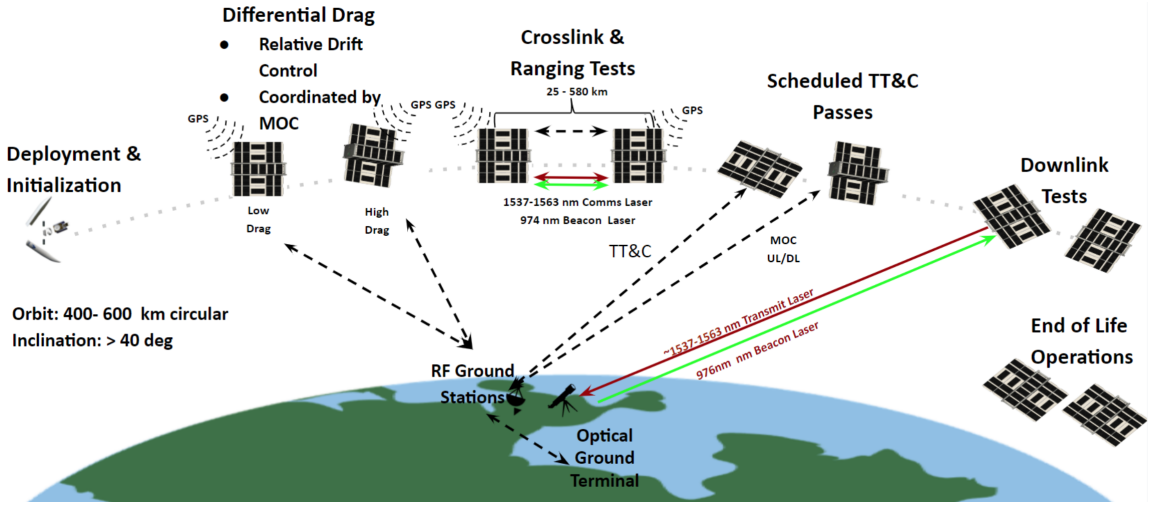

Figure 1-13: CLICK-B/C concept of operations.

1.4 Thesis Structure

This thesis describes the thermal and thermoelastic analysis of the CLICK-A and -B/C payloads. The thermal analysis is used to predict the on orbit temperature of the components in each payload. These temperatures are compared against their stated and determined survival and operational temperature limits. The thermoelastic analysis provides estimates in the thermoelastic shift for the CLICK-B/C optics to provide an upper bound on the misalignment pointing error induced during operation of the payload. The reason CLICK-A is not included in this thermoelastic analysis is because the current thermoelastic error prediction for CLICK-A was defined to be negligible compared to other pointing disturbances [26].

Chapter 1 provides context for this thesis and describes the relevant topics to provide background to the work performed. The concept of CubeSats and optical communication are described, as well as a brief introduction of the CLICK mission and the payloads that comprise it. Chapter 2 provides a description of the thermal

design of the CLICK payloads. The components that comprise each of these payloads are listed with the temperatures that they must be maintained within. The overall approach to how these temperatures are maintained is described. Chapter 3 describes the development of the thermal model of the CLICK payloads. Included in this chapter are the considerations that are important in the modeling of the payloads to calculate predicted on orbit temperatures. The results of the models are compared to the temperatures that must be maintained for the various components of the payloads. Chapter 4 describes the development of the thermoelastic model for the CLICK-B/C payload. The approach to predicting the thermoelastic deformation of the optical mounts is discussed. The importance of predicting the thermoelastic deformation for the fine pointing budget of the payload is discussed. Chapter 5 summarizes the work completed in the thesis, including the contributions, and future work needed in the development of the CLICK payloads.

Chapter 2

Thermal Design of CLICK Payloads

To meet CLICK mission requirements, the components in the payloads must be kept within their operational temperature bounds when the payloads are active. Since the payloads are nominally off when preparing to transmit, the components must be kept within their survival temperatures while the payload is turned off.

The thermal environment for objects in low Earth orbit (LEO) can vary depending on orbit and object configuration. The heating due to solar energy, reflection of solar energy off the Earth (called albedo), the infrared heating due to the temperature of the Earth, the spacecraft internal heat sources, and heat loss to space must be taken into account [27]. There is a thermal balance happening where the object is being heated by the various heating factors, while also losing thermal energy through infrared radiation to deep space. When the object enters the shadow of the Earth, the only heating environmental factor left is the infrared heating from the Earth. Given the low altitude of the orbit (e.g. 400 km of ISS orbit), the fraction of the amount of an orbit the object spends in eclipse can vary from 0 to 0.4 [27]. This fraction plays a large role in the temperature swings experienced in the LEO environment. Due to the nature of how the CLICK payloads are integrated to their host spacecraft which has its own thermal management system, the thermal design does not have to explicitly account for all of the various factors that lead to the dynamic thermal environment of low Earth orbit. Since the payloads are completely housed by the spacecraft bus, the temperature of the sides of the spacecraft bus are the boundary

conditions of that the thermal design references, which are defined by a maximum and minimum bus-payload interface temperature. The range of the maximum and minimum temperature is largely dependent on the dynamic LEO environment. For CLICK this is coordinated with and defined by the bus provider, in the payload-to-bus interface control document A9SP-1803-XR003 Rev. G.

2.1 CLICK-A Payload Thermal Design

The thermal environment of the CLICK-A payload is managed by the payload payload thermal control system (TCS). The TCS monitors the temperature of most components in the payload and maintains the temperature of a subset those components. The temperatures of components are monitored through resistance temperature detectors (RTD). The RTDs used are the Honeywell HRTS-5760-B-U-0-12. These sensors are mounted on the monitored components using 2216 epoxy and allow the TCS to measure what temperature these components are when the payload is operating. The TCS is primarily passive, meaning that it is designed to keep temperatures within their operational temperature bounds without the need for actively applying extra heat to components during operation of the payload, except for heaters for the EDFA and TOSA components. The passive thermal design is ideal since it means that a platform like a 3U CubeSat does not need to overutilize the limited power available.

Another important aspect of the thermal design is to try to sink heat away from components that generate a large amount of heat relative to the rest of the payload. The exact amount of heat being dissipated by each component in CLICK-A is described in the Chapter 3. The main component of concern was the Raspberry Pi computer since it generates a large amount of heat and has very poor thermal paths to conduct heat away. Due to the fiber raceway being located directly underneath the Raspberry Pi, the addition of gap filler between the main chip of the Raspberry Pi and the fiber raceway allows a convenient path to heat sink away. Since the fiber raceway has an aluminum cover, which is mounted near the rails of the structure, it can easily transfer heat and allow the Raspberry Pi to not overheat.

2.1.1 CLICK-A Components Temperature Ratings

The temperatures that the components must be maintained to are initially derived from the component data sheets, and then tested in thermal vacuum (TVAC). For each of the custom electronic boards, the components that make up the board each had their data sheet inspected for the survival and operational temperature ranges. Certain critical components lacked operational and survival temperature ranges, so these were tested to obtain usable values. A list of the of the components in the CLICK-A payload with their operational and survival temperatures is shown in Table 2.1. It can be seen that in terms of operational temperature limits, the feedback laser and the EDFA have the highest minimum operational temperatures (most restrictive). These components are important in evaluating the lower interface temperature bound of the payload to the bus.

Table 2.1: Survival and operational temperature limits of CLICK-A components.

Component:	**Temperature Limits of Each Component (°C)**			
	Survival		**Operational**	
	Min	**Max**	**Min**	**Max**
Daughter Board	-55	125	-25	85
FPGA Board	-40	125	-40	85
Photodiode Board	-40	85	-40	85
CPU Board	-55	125	-40	85
TOSA Board	-40	85	-5	75
Feedback Laser	-35	80	0	60
EDFA	-20	65	0	65
Camera	-40	60	-40	45
FSM	-40	125	-40	125

Initially, there were components of the daughter board, FPGA board, and CPU board that were not selected to be industrial grade parts and these limited the operational temperature ranges for the boards. Those parts were replaced with their industrial equivalents to support a larger operational temperature range. The daughter board, FPGA, and CPU boards especially needed to have industrial parts to work given the interface of the payload to the bus, and their role in the operation of the heater control of the payload.

2.1.2 TVAC Testing of Beacon Camera and Lens

Not all the values in Table 2.1 are derived from data sheets. The camera that is used to acquire and track the beacon has a minimum operational temperature of 0°C according to its data sheet [28]. We tested the performance of the camera and lens in a thermal vacuum chamber to mimic the space environment to determine how the vacuum and range of temperatures affected the optical performance of these components. To perform this test, the structural components of the CLICK-A payload were attached to an adapter plate that was used to mount the structural components inside the vacuum chamber. This adapter plate matched the bolt pattern of the back plate of the CLICK-A structure. The structure of the CLICK-A payload was used for this test since it is already designed to hold the the camera and lens components. The temperature gradients between the camera and lens during the test should also mimic the gradients expected during operation on orbit since they are mounted in the same structure. The mounted camera and lens, attached to the CLICK-A payload structural components and adapter plate, is shown in Figure 2-1a. The chamber that was used, along with the test equipment, is shown in Figure 2-1b. The test equipment shown mounted above the chamber is used to send collimated light into the chamber window. This work was performed in the MIT Kavli Institute with the phenomenal help of Joel Villasenor.

This TVAC test was run twice in December 2019, across two different temperature ranges. The vacuum of the chamber was measured down to 1E-5 Torr for both trials. The first trial was from -20°C to 40°C. The second trial was from 50°C to -35°C. The

temperature profiles for the tests can be seen in Figure 2-2 and in Figure 2-3. These trials were able to demonstrate the successful operational performance of the camera and lens down to -35°C and up to 45°C. Issues start occurring around 50°C when the camera would randomly shut down. The test for trial 2 only had the camera operating, and involved taking images to assure the optical performance once the camera reached 50°C.

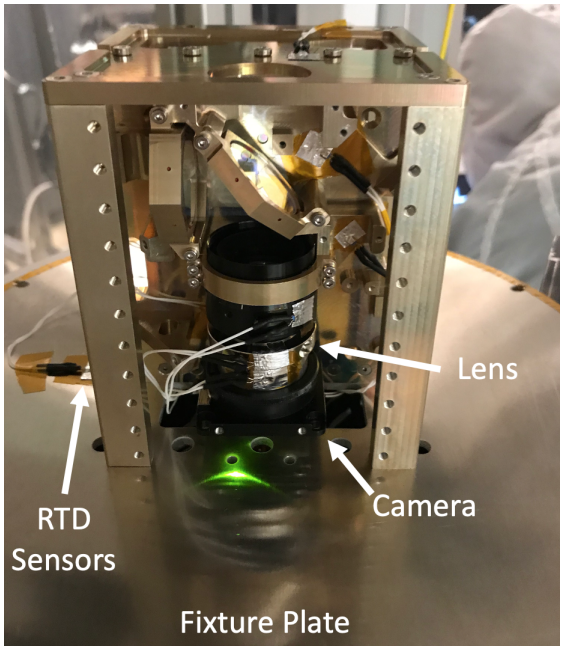

(a) Setup for CLICK camera and lens TVAC test.

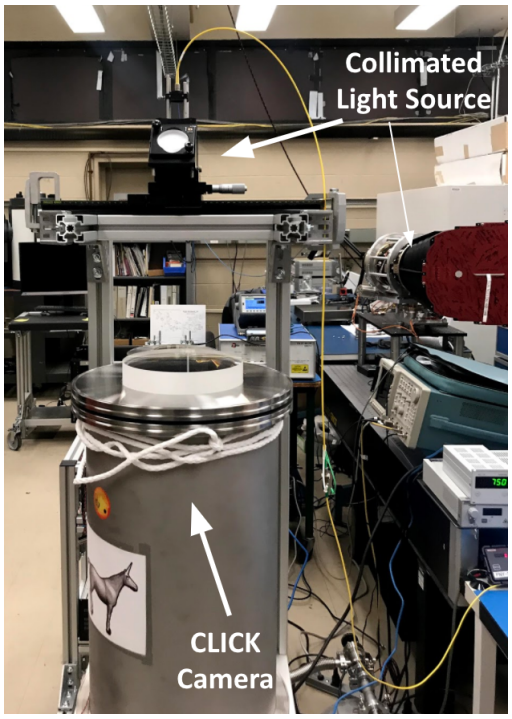

(b) Chamber and test equipment used in CLICK TVAC test. Camera and lens assembly mounted inside chamber.

Figure 2-1: Pictures from the TVAC testing of the beacon camera and lens in the MIT Kavli lab in December 2019.

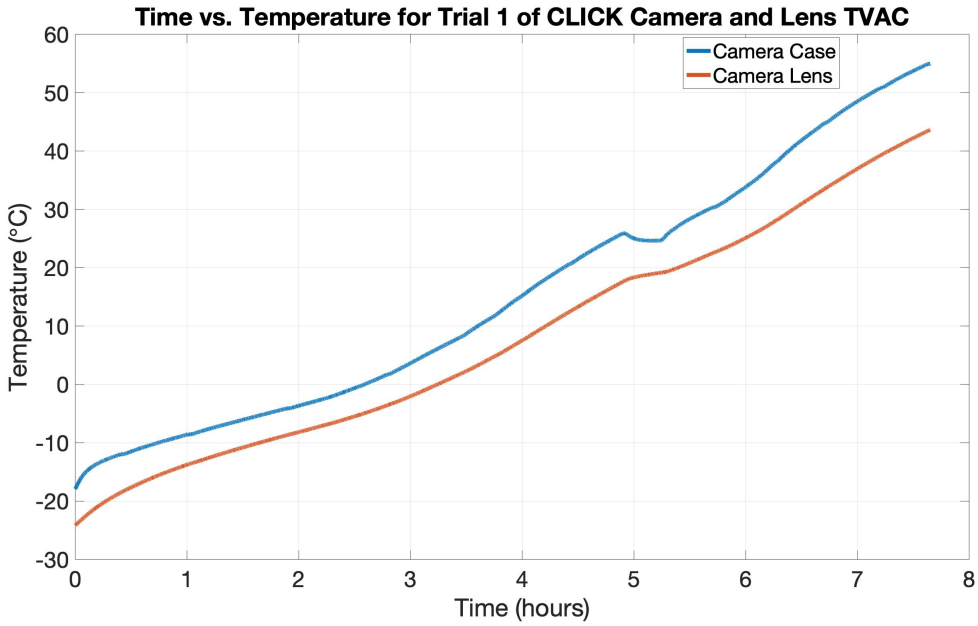

Figure 2-2: Temperature vs. time for the CLICK camera and lens TVAC trial 1. December 2019. MIT Kavli Institute.

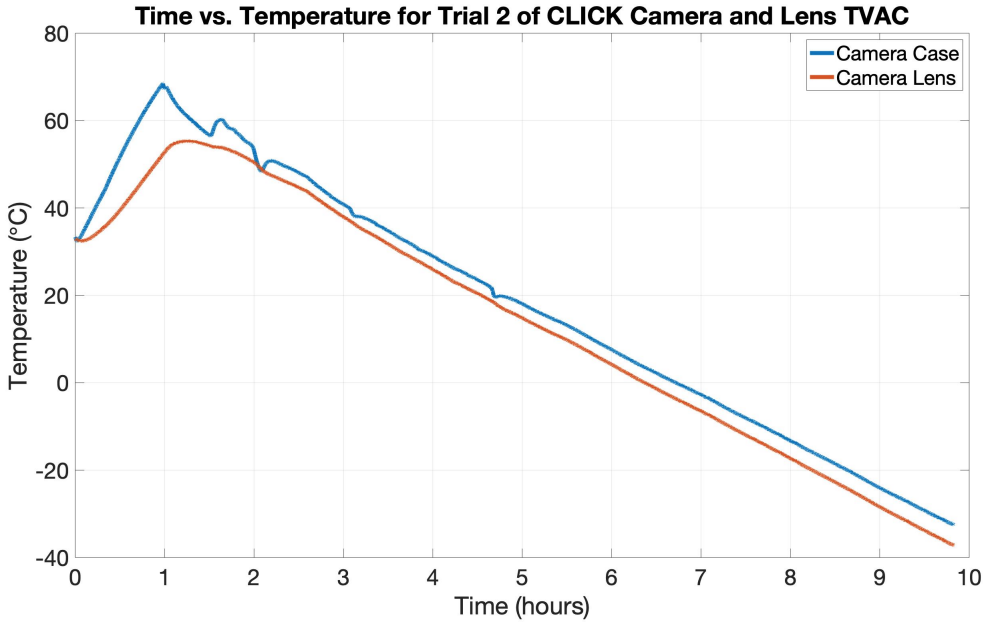

Figure 2-3: Temperature vs. time for the CLICK camera and lens TVAC trial 2. December 2019. MIT Kavli Institute.

2.1.3 Payload Heater Options

While the thermal control system is primarily passive, active components are used if the expected temperature of components does not stay within the relevant temperature bounds during that portion of the mission. The ability to actively lower the temperature of components on orbit is available by using cooling units such as cryocoolers and thermoelectric coolers, although these are not common on CubeSats since these components are complex and their efficiencies are quite low.

The ability to raise the temperature of components is relatively easy, compared to cooling, through the use of resistive heaters. These heaters use Joule heating, where a current is passed through a component designed with a specific resistance and at a certain voltage. The heaters used on spacecraft often are polyimide heaters, a thin film piece of polyimide with an etched foil to produce a very long conductive path. An example of one of heaters used for CLICK-A is shown in Figure 2-4. This long path can be tuned for a specific resistance. These heaters can be attached on or near components that require their temperature increased. Polyimide heaters are typically specified to operate with voltages of 12 V, 28 V, or 115 V. These design voltages are used along with the resistance of the heater to draw the current needed to generate a prescribed heater power. For the CLICK-A payload, the voltage available for the heaters is 5 V. For most consumer heaters, the difference between the available payload voltage and the design voltage causes the power dissipation rates at the available payload voltage to be too low to be usable in a thermal control system. The ideal resistance values for a heater for CLICK-A would be between 5-15 ohms. This would produce a heat dissipation of 5 to 1.66 Watts. After an extensive search, there were six candidate heaters identified. The two companies that were able to offer heaters with the correct resistance were Birk and All Flex Inc.. The heater options with the required resistance is shown in Table 2.2.

The heaters were chosen through the modeling of the payload in Thermal Desktop, as described in Chapter 3, and iterating on the amount of heater power that is needed to be applied to heat components to their operational temperature.

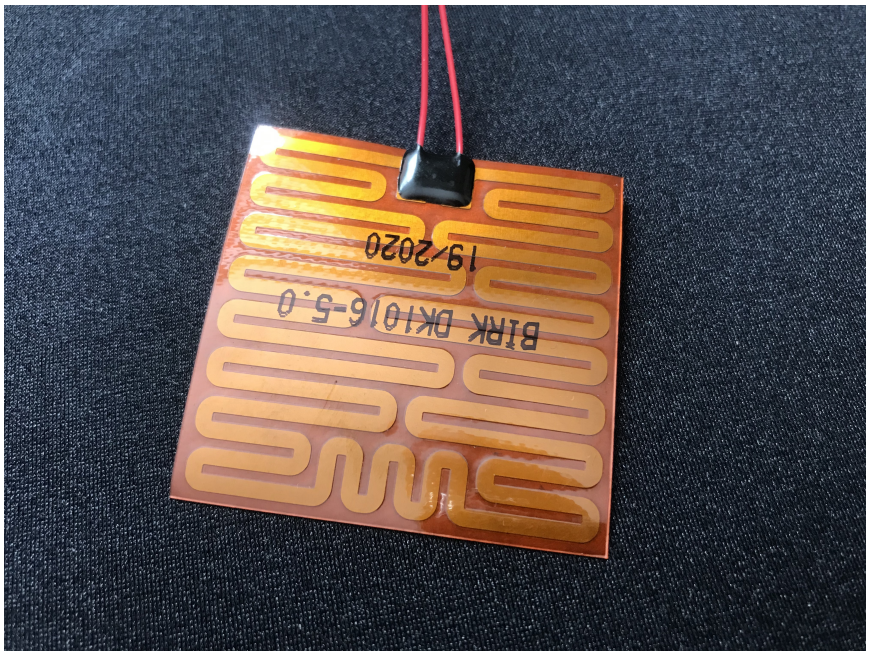

Figure 2-4: Polyimide heater typically used to heat components on satellites. This specific heater is used on the CLICK-A EDFA and is a Birk DK1016-5.

Table 2.2: Heater options for the CLICK-A payload.

Manufacturer:	**Part Number:**	**Size:**	**Resistance: [Ohms]**	**Power at 5V [W]:**
All Flex Inc.	AF-PR1.00-1.00S1P5.50-12.00	1.0 in. by 1.0 in.	5.5	4.55
All Flex Inc.	AF-PR1.00-0.50R7P12.50-6.00	1.0 in. by 0.5 in.	12.5	2.00
All Flex Inc.	AF-PR3.00-1.50R8P9.00-12.00	3.0 in. by 1.5 in.	9	2.78
Birk	DK1014-5	1.5 in. by 1.5 in.	12.8	1.95
Birk	DK1016-5	2.0 in. by 2.0 in.	7.2	3.47

2.2 CLICK-B/C Payloads Thermal Design

The similar mechanical design and interface between CLICK-A and -B/C means their thermal design is also very similar. The thermal environment of the CLICK-B/C payload is managed by the payload thermal control system (TCS). The TCS monitors the temperature of most components in the payload and maintains the temperature of a subset those components. The CLICK-B/C payloads use the same resistance temperature detectors (RTD) as CLICK-A. These sensors are mounted on the monitored components using 2216 epoxy and allow the TCS to measure what temperature these components are when the payload is operating. The TCS is primarily passive, but uses heaters on the EDFA since this component has the highest minimum operational temperature.

CLICK-B/C also uses gap filler in certain areas, such as the FPGA board, Raspberry Pi computer, and optoelectronics board to sink heat away. CLICK-B/C has a heat spreader for the FPGA board since the power it draws is quite high compared with its ability to dissipate heat. The aluminum heat spreader conforms to the mechanical design of the FPGA board and has pedestals that are designed to sit very close to the parts of the FPGA board that dissipate the most. Gap filler will be used between the pedestals and the FPGA. This heat spreader is mounted to the back plate of the payload to sink heat into the structure of the payload. There is also another heat spreader attached to the Raspberry Pi on the back of the payload. The Raspberry Pi component needs the heat spreader mainly due to the lack of thermal paths to conduct heat away during operation. The heat spreader provides a thermal pathway and is connected to the Raspberry Pi thermally through gap filler. A picture of the preliminary Raspberry Pi heat spreader is shown is in Figure 2-5.

2.2.1 CLICK-B/C Components Temperature Ratings

As with the CLICK-A payload, the temperatures that the components must be maintained to are derived from the components data sheets whenever possible. Due to the less mature design of the CLICK-B/C payload compared with the CLICK-A pay-

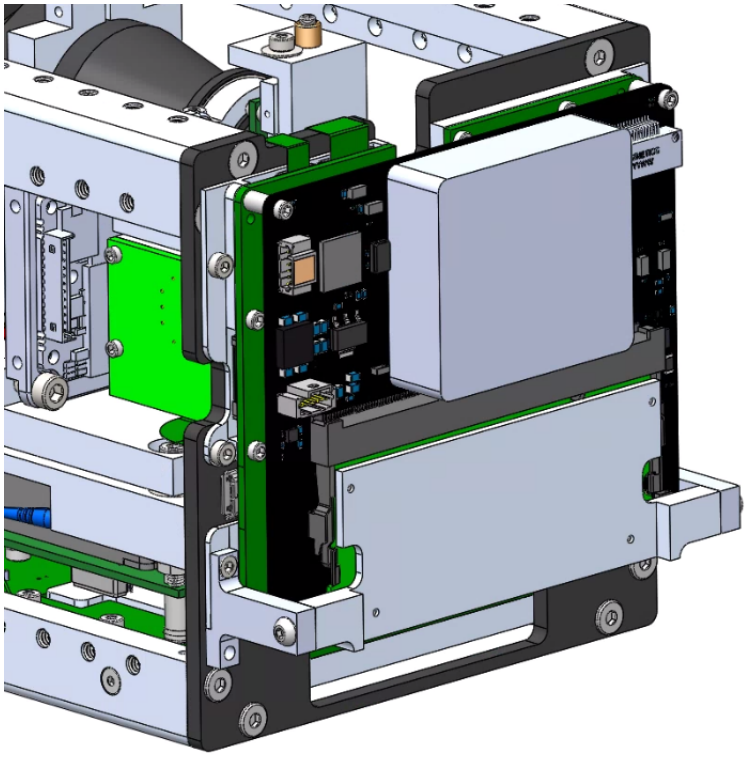

Figure 2-5: CLICK-B/C Raspberry Pi heat spreader from V1.4 CAD model.

load, some of the survival and operational temperature ranges for components are estimated. As the design develops further and component selection is completed for the custom boards of the payload, the survival and operational temperature ranges will be updated. As a starting point, the estimates are based on typical industrial component temperature ranges. CLICK-B/C has benefited from the lessons in designing CLICK-A, and started by selecting all industrial grade parts whenever possible. The CLICK-B/C payload also benefits from using some of the same components as the CLICK-A payload, most notably the beacon camera and lens. As with CLICK-A, certain key components will be tested in TVAC to validate the operational temperature bounds for the components. The CLICK-B/C mission is planning to do TVAC testing of the engineering design unit to validate the thermal model of the payload. A table of the of the components within the CLICK-B/C payload is shown in Table 2.3. It can be seen that in terms of operational temperature limits, the CPU board and the EDFA have the highest minimum operational temperatures (most restrictive).

Table 2.3: Survival and operational temperature limits of CLICK-B/C components.

Component:	**Temperature Limits of Each Component (°C)**			
	Survival		**Operational**	
	Min	**Max**	**Min**	**Max**
Daughter Board	-55	125	-40	85
FPGA Board	-55	125	-40	85
APD Board	-55	125	-40	85
CPU Board	-55	85	-10	70
Optoelectronics Board	-55	125	-40	85
Quadcell Board	-55	125	-40	85
EDFA	-20	65	0	65
Camera	-40	60	-40	45

2.2.2 Optical Bench Thermal Isolation

The CLICK-B/C optical bench, as described in Section 1.3.2, is separated from the main structure of the payload for ease of assembly and alignment of the optics as well as to provide thermal isolation. The main motivation for the thermal isolation is to try to reduce the thermoelastic shifting of the optical bench from heating due to the plate it is mounted to. The plate the optical bench is mounted to is also the mounting location for the EDFA. The EDFA outputs between 5-6 Watts while operating, and given the how the EDFA is heat sunk to its mounting plate, as it is in CLICK-A, the EDFA mounting plate will heat up quickly. Titanium thermal isolators were implemented to create a large thermal resistance between the mounting plate and the optical bench to limit heat transfer between the two.

The thermal isolator design is inspired from the Spacecraft Thermal Control Hand-

book [27], and reflects the design from Figure 8-60 from the chapter on mountings and interfaces, which is replicated here in Figure 2-6. It can be seen in Figure 2-6 that the thermal pathways are broken into two distinct routes, one is along the long path of the bolt and the other is through the center isolator. The design from Figure 2-6 was implemented for the CLICK-B/C optical bench thermal isolator as closely as possible, given other design constraints on the optical bench. The other constraints that have hindered the optical bench thermal isolator design are the location of where to put the thermal isolators, and how certain components were not able to be moved from occupying those locations. Due to the interference with certain components, not all of the thermal isolators between the optical bench and EDFA plate contain all three spacers. There are 5 thermal isolators total. The back two being the design the three spacers, which is also the location on the optical bench most susceptible to thermoelastic shifts. The current engineering design unit has been manufactured with these isolators, and the Chapter 4 will assess whether they need to be revised or not.

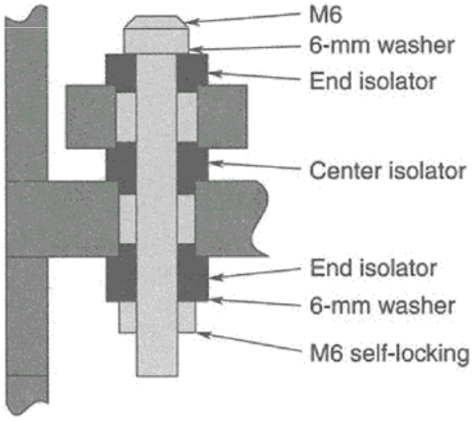

Fig. 8.60. Thermal isolation at bolted-joint interface.

Figure 2-6: Inspiration for CLICK-B/C optical bench thermal isolator design [27].

Another form of thermal isolator that CLICK-B/C may use is similar to the feet that held the optical bench of another CubeSat mission from MIT STAR Lab called DeMi, or the Deformable Mirror Demonstration Mission, which launched in February of 2020. The thermal isolators, which are shown in Figure 2-7, provide a

long conduction path for heat from the bus to the optical bench, but come at the cost of being much larger and more massive compared to the previous design. The thermal isolators for DeMi are also made out titanium, which has one of the lowest thermal conductivities of any metal.

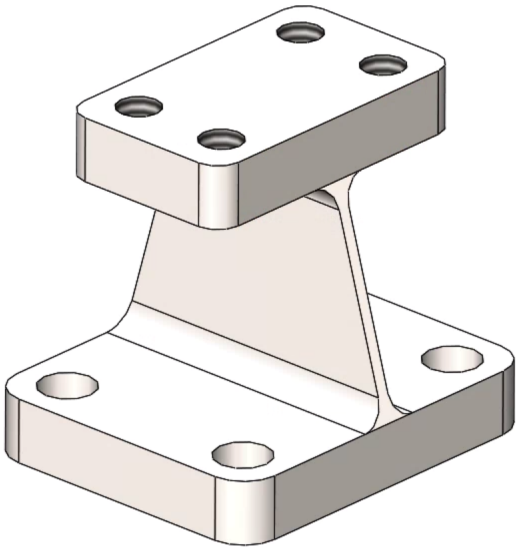

Figure 2-7: Thermal isolators used on DeMi mission. Source: DeMi CAD model.

2.3 Thermal Design Summary

This chapter has explained approach to the thermal design of the CLICK-A and CLICK-B/C payloads. A description of how the thermal control systems monitor and maintain temperatures for each payload is discussed. The thermal design choices to ensure the operation of the payload is explained and motivated. The determination of component temperature ratings is explained, as well as the TVAC testing that was performed on critical components to determine their space survivability and performance. The next chapter will explain how this design is modeled and how the on orbit temperatures of the components in the CLICK-A and CLICK-B/C payloads are predicted.

Chapter 3

Thermal Model Development and Results

The goal of the thermal model discussed in this chapter is to provide predictions of the temperature of components while operating on orbit. This chapter will go over relevant factors for building a thermal model and how to implement them into the thermal model for the two lasercom payloads.

3.1 Thermal Desktop

Thermal Desktop is software that runs a numerical solver called SINDA/FLUINT. SINDA stands for Systems Improved Numerical Differencing Analyzer, while the FLUINT parts stands for Fluid Integrator [29]. SINDA/FLUINT has a long history of development dating all the way back to the 1960's when the original CINDA code was developed by Chrysler Aerospace. It was further developed by NASA until it was commercialized during the early 1990s through Cullimore and Ring Technologies [30]. Cullimore and Ring Technologies has been further developing the numerical solver of SINDA/FLUINT, but most of that is hidden behind a graphic user interface (GUI) called Thermal Desktop. Thermal Desktop is used to set up the input files for SINDA/FLUINT. The SINDA/FLUINT numerical solver can solve both finite difference and finite element equations. Finite difference solid and surfaces are used

to represent most of the components that make up the thermal network. Surfaces are used instead of solids when the thermal gradient through the thickness of a component is not important. Finite elements are primarily used to represent complex geometry and there are a variety of ways of building a finite element mesh for Thermal Desktop. The thermal models for the CLICK-A and -B/C payloads were built in the Thermal Desktop GUI for the SINDA/FLUINT solver to compute. The inputs into the thermal model will be described in the sections below.

3.2 Material and Optical Properties

The mechanical design of these payloads is done in Dassault Systèmes SolidWorks software. The design is represented within a model that is called the CAD model or computer aided design model and is used in the manufacturing of the mechanical components that make up the payloads. The CAD model defines the geometry and material of the various parts that compose the payload. Due to the way that the Thermal Desktop modeling process works, the CAD model cannot be imported into the Thermal Desktop without adding unnecessary complexity to the model. The thermal model is built by referencing the CAD model components and building their thermal equivalent in Thermal Desktop. The primary shapes that can be used to represent components are finite difference 2D surfaces (rectangles and circles), or 3D simple shapes (rectangular prisms, cylinders, cones, and spheres). When dealing with the simple shapes allowed within Thermal Desktop, the CAD model must usually be simplified to be represented by these simple shapes. While the exact geometry does not always matter, representing the correct thermal capacitance of an object is usually what is favored since it can dictate how heat flows into and out of a model. The components modeled have a certain amount of thermal capacitance based on their thermal properties and geoemetry. The thermal properties of the materials that the payload is made of must be imported into Thermal Desktop and include the conductivity (both isotropic and anisotropic is allowed), specific heat, and density of the material.

For the CLICK payloads, the majority of the model is made of Aluminum 6061-T6. The optics are modeled as fused silica material and the electronics are modeled as a printed circuit board (PCB) material. A list of the materials used in the CLICK-A and -B/C thermal models is shown in Table 3.1.

Table 3.1: Material properties used in CLICK-A and -B/C thermal models.

Material:	**Conductivity: [W/mm-K]**	**Specific Heat: [J/kg-K]**	**Density: [kg/mm^3]**	**Source:**
Aluminum 6061-T6	0.167	896	2.70E-06	[31]
Fused Silica	0.00135	728	2.21E-06	[32]
PCB-FR4	0.004	1000	1.83E-06	[33]

The material properties described in Table 3.1 are used to defined the conductive thermal network within the model. The model also takes into account the infrared (IR) radiation between components. The geometry that is modeled is used to define the component's thermal capacitance as well as to perform a Monte-Carlo ray tracing analysis to determine the view factors between components. Also needed for the radiation calculations are the optical properties, which are used to define the solar absorptivity and the IR emissivity. Optical properties can vary based on coatings and how surfaces are treated. Bare aluminum can have a large range of values for emissivity and absorptivity, depending on how the metal is finished [27]. One of the ways of dealing with this uncertainty is to apply a coating to the metal to create a known surface that has been characterized in literature. The coatings for CLICK-A and -B/C were not chosen for solely their optical properties, given the small amount of area for a >2U payload. The CLICK-A payload has an alodine chromate coating (MIL-DTL-5541 Class 3) while the CLICK-B/C payload has a clear anodization coating. The panels that enclose the both payloads are provided by the bus provider and they have given the optical properties of the coating that the panels will have. The name of this coating is called iridite aluminum. The printed circuit boards in the

model use general optical properties values since the solder mask used for the board can vary the optical properties. A list of the optical properties used in the CLICK-A and B/C thermal models is shown in Table 3.2.

Table 3.2: Optical properties used in CLICK-A and -B/C thermal models.

Optical Property:	**Absorptivity:**	**Emissivity:**	**Source:**
Alodine on Aluminum 6061	0.33	0.07	[34]
Printed Circuit Board (G111)	0.6875	0.855	[34]
Iridite Aluminum (BCT Panels)	0.25	0.06	BCT Thermal Engineer
Black Anodize	0.86	0.86	[27]
Clear Anodize	0.27	0.76	[35]

3.3 Conductors

A conductor is used to represent a heat flow path between components in a thermal model. The ability of a conductor to transfer heat from one node i to another node j is called conductance. The heat transfer rate between two components connected by a conductor is defined in Equation 3.1 [27]. The rate of heat transfer is $\dot{Q}$ (W), G (W/K) is the conductance between the two nodes, and the T (K) is the temperature of node i and node j.

$$\dot{Q} = G_{ij}(T_i - T_j) \tag{3.1}$$

The calculation for conductance through a homogeneous material is defined in Equation 3.2 [27]. The k (W/m-K) is the thermal conductivity of the material, A (m^2) is the cross-sectional area perpendicular to the direction of the heat flow, and L (m) is the length of the conductor from node i to node j.

$$G_{ij} = \frac{kA}{L} \tag{3.2}$$

All the mechanical connections within the design of the payload must be represented in the thermal model. Most connections between components are mated together through a bolt. For small CubeSat programs, such as the CLICK program, the bolt conductance values are usually not calculated, though larger NASA programs tend to perform this characterization. A table of standard bolt conductance values based on the size of bolt is used instead. The bolt conductance value table referenced in the building of the thermal models described in this chapter is Table 8.4 from Spacecraft Thermal Control Handbook and is replicated in Figure 3-1 [27]. The majority of the bolts that comprise the mechanical connections in the payload are M2.5 and M3 bolts, which were approximated as 4-40 bolt conductance values connecting small stiff surfaces. The bus provider uses a conductance of 0.2 W/K for their 4-40 bolted connection, and this was used in the model for the interface bolts between the payload and the spacecraft bus.

Table 8.4. Thermal Conductance Design Guideline from TRW

	Conductances (W/K)	
Screw Size	Small Stiff Surfaces	Large Thin Surfaces
2–56	0.21	0.105
4–40	0.26	0.132
6–32	0.42	0.176
8–32	0.80	0.264
10–32	1.32	0.527
1/4–28	3.51	1.054

Figure 3-1: Conductance values for various bolts used in thermal model from Spacecraft Thermal Control Handbook [27].

3.4 Transient Heat Loads Modeling

The previous sections discussed important aspects of representing the thermal network of the payload correctly, including the modeling of the correct thermal capacitance, optical properties, and conductors. Another important aspect in building thermal models is modeling the amount of heat going into the system with the transient pattern that reflects the concept of operations of the payload.

The CLICK team discussed what the operation of the two payloads will look like while each is operating. The payloads are nominally off unless they are about to perform a transmission. The modes of operation are as follows: startup, transmit, power down. The spacecraft is able to control the power supplied to the payload to allow it to turn on and go into startup mode. In startup mode, the payload is evaluating the performance of its various systems and preheating certain components if necessary. The spacecraft will then issue commands begin transmit mode to begin the beacon tracking and transmission of modulated light from the payload. After a certain transmission duration, the payload will then stop transmitting and go into a power down mode, where the payload sends the telemetry generated during the overpass transmission. The telemetry contains performance metrics (temperatures of components, in-fiber photodiode power levels, etc.) of the payload over the transmission time.

To determine the duration of each operating mode of the payload, the team considered what would happen within each mode. For startup, 10 minutes is used as a baseline time, and then updated later after analysis of the amount of time for the payload to preheat itself for transmit mode. Section 3.6 will expand upon this more later. The transmit mode has to do with what each payload does during a transmission, whether to the ground, or a crosslink transmission.

To determine the length of the transmission mode for the CLICK-A payload, the following approach is used. The period of a satellite in an ISS orbit was calculated using Kepler's third law, defined in Equation 3.3. The T (s) is the period of the orbit, the a (km) is the semi-major axis, the G (m^3/kg-s^2) is the gravitational constant of the Earth, and the M (kg) is the mass of the Earth. The period was calculated to be

5,556 seconds for an orbit with an altitude of 409 km.

$$T = 2\pi\sqrt{\frac{a^3}{GM}} \tag{3.3}$$

Next, the amount of time that the satellite will be visible to the ground station for a downlink needed to be determined. Figure 3-2 shows what the horizon looks like for an ideal overpass of the ground station, with ideal meaning the satellite passes at an elevation angle of 90° overhead. There is a right triangle formed between the center of the Earth, the ground station location and the point where the satellite crosses the horizon. To solve for the angle (θ) that represents half of the amount of the orbit that the satellite is visible to the ground station, Equation 3.4 was used. The R_{Earth} is the radius of the Earth (km), which is 6371 km, and the *Altitude* (km) is the orbital altitude of the orbit being calculated, which is 409 km in this calculation.

$$cos(\theta) = \frac{R_{Earth}}{R_{Earth} + Altitude} \tag{3.4}$$

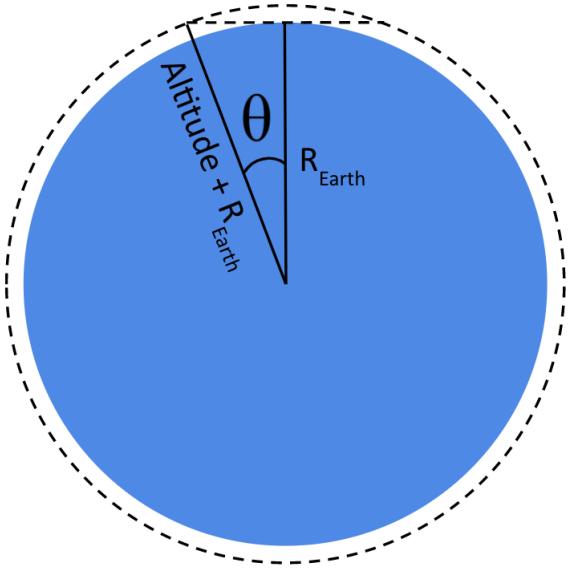

Figure 3-2: Geometry used in overpass duration calculation.

The angle calculated for an ISS orbit is 20°, so 40° is used for the total overpass amount. Since the full orbit is 360°, we know can calculate the amount of the orbit that the satellite is visible, with dividing 40° by 360° to get 11.1% of the orbit is

visible. Multiplying the percent of the orbit that the satellite is visible to the ground station by the total period time, the maximum amount of time that the satellite will be visible is 617.41 seconds or 10.29 minutes. Now, it is known that the ground station will not be able to see the light at the horizon due its extended range from the ground station and the trees that are at the ground station sight will limit the angles where the ground station can track, but this number does give a maximum theoretical amount of time that the laser could be seen by a more sensitive ground station. The CLICK team decided to bump the transmit time to 15 minutes, to have some buffer time before and after the transmit to verify the functionality of the full optical fiber train. For the CLICK-B/C payloads, the duration of a crosslink transmission is not dependent on the same orbital geometry that the operation of the downlink of CLICK-A is dependent on. The only orbital situation that could preclude a crosslink transmission has to do with the angle of the Sun with respect to the payload. Our team has added a baffle to the beacon camera with a 46.5° Sun-keep-out half-angle to improve the standard 10° field of view of the camera lens, but it is assumed that Sun-keep-out angle will not be violated for the transmission in the thermal model. The duration of a crosslink is largely dependent on the amount of power available by the spacecraft. The team chose to have a transmit operation last 15 minutes, the same duration as used for the CLICK-A payload. The bus provider will inform the CLICK team whether the power budget for the spacecraft can support a transmit duration this long, but thermally the worst case will be a 15 minute duration. The next mode involves preparing the payload for being shut down. The payload enters a mode called power down, where it is no longer transmitting light, but instead communicating performance metrics of how the payload performed during the previous activity to the bus. These metrics are stored on the bus for later downlink via the radio link. The power down mode was given 5 minutes to transfer all the data over the spacecraft.

Now that the duration of each mode was defined, the amount of heat that each component is dissipating must be determined. To determine these amounts, two methods are used. For the start up and power down modes, the components are

turned on and the amount of power that they draw is recorded. For the transmit mode, the amount of power drawn by each component is estimated by the electrical engineer who designed the boards [36]. For the model described in this thesis, only the CLICK-A boards were able to be evaluated for power draws by turning the actual components on. The active components and the amount of power they draw for the CLICK-A payload is shown in Table 3.3 and in Table 3.4 for CLICK-B/C. It can be seen that the total transmit mode power draw for the CLICK-B/C payload is roughly 50% more, which is due to the -B and -C payloads both transmitting and receiving communication signals.

The heat loads are defined by the different modes of operation, but it also matters when during the orbit the payload turns on. It depends on the whether the hot case or the cold case is being run, but the rule of thumb is to set the up the payload to turn on during a time that will stress the temperature bounds as much as possible. For the cold case, this means turning on the payload at the coldest point of the cold case orbit. This ensures that even in the coldest state, the payload will be able to preheat sufficiently. For the hot case, this means turning on the payload at the hottest point of the hot case orbit. This will be expanded on more in Section 3.5.

Table 3.3: Heat loads for the modes of CLICK-A payload downlink transmission.

Component:	**Power Draws (W) for Each Mode**		
	Start Up (10 Minutes)	**Transmit (15 Minutes)**	**Power Down (5 Minutes)**
Daughter Board	0.4	2	0.4
FPGA Board	1.1	2	1.1
Photodiode Board	0.35	1	0.35
CPU Board	1.5	2	1.5
TOSA Board	0.15	1	0.15
Calibration Laser	0	1	0
EDFA	0	6	0
Camera	0.45	1	0.45
Heaters	5	0	
Total	**8.95**	**16**	**3.95**

Table 3.4: Heat loads for the modes of CLICK-B/C payload crosslink transmission.

Component:	**Power Draws (W) for Each Mode**		
	Start Up (10 Minutes)	**Transmit (15 Minutes)**	**Power Down (5 Minutes)**
Daughter Board	0.5	1	0.5
FPGA Board	0	5.45	0
APD Board	0	2	0
CPU Board	2.53	2.84	2.53
Optoelectronics Board	0	6.39	0
EDFA	0	6.39	0
Camera	0	1	0
Heaters	10	0	
Total	**13.03**	**23.88**	**3.03**

3.5 Transient Boundary Conditions

The thermal model is not complete without taking into account the boundary conditions of the model. If the thermal model was modeled in the space environment, then the orbit of the spacecraft must be taken into account. The beta angle, which is the angle between a satellite's orbital plane and the solar vector, must be accounted for, since it determines the time spent in sun and eclipse, which is directly related to the amount of solar heating a satellite experiences in orbit. One of the many powerful aspects of Thermal Desktop is its ability to model the thermal environment of space. The user needs to input the orbital parameters into the model, mainly altitude and Beta angle, and the software is able to determine heating loads for the various heating factors that are dominant in the LEO orbit (solar, albedo, and Earthshine heating). Due to the nature of how the CLICK payloads were designed to be incorporated in the spacecraft bus, the thermal models built for this thesis do not model the payload in an orbital environment. Instead, the bus provider runs their thermal model with a CLICK payload like thermal mass and heating rate included, which is used to provide

temperatures of the interfaces between the bus and the payload. The bus provider is able to provide what the temperature of the spacecraft interface faces will be both while the payload is off, and while the payload is on and dissipating the heat loads described in the Section 3.4. The boundary conditions are physically modeled the same in each model. A figure of the CLICK-B/C spacecraft CAD model payload encapsulation, compared to the model boundary conditions is shown in Figure 3-3.

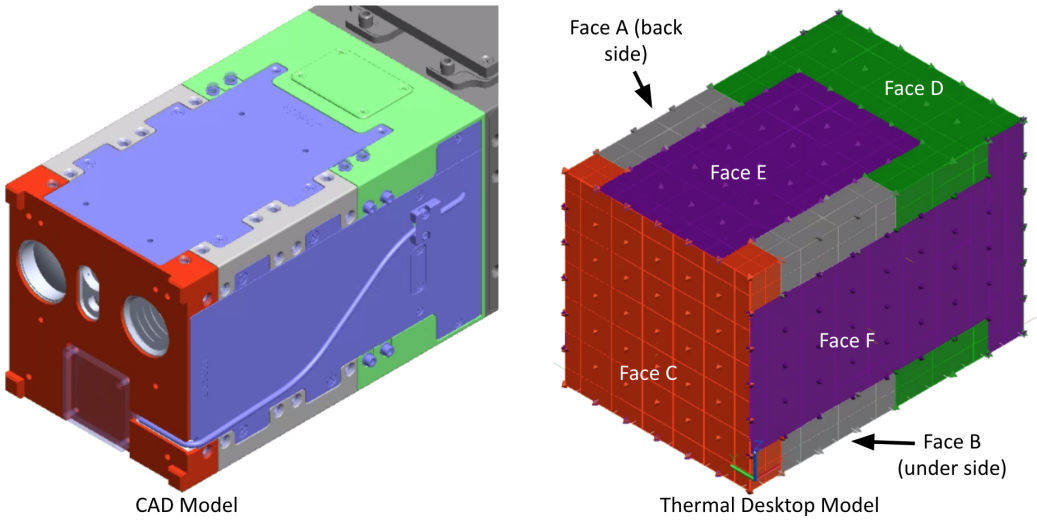

Figure 3-3: CLICK-B/C spacecraft CAD model of payload enclosure compared to the boundary conditions modeled in the thermal model. Faces used to define temperature of mechanical interface labeled.

The start of determining the interface between the payload and the spacecraft is to determine what the maximum and minimum temperature range of the payload mechanical interfaces would be to accommodate the payload temperature requirements. For CLICK-A, there was a different approach for determining each extreme of the temperate range.

For the CLICK-A maximum interface temperature, the maximum operational and survival temperature limits of each component are considered. The maximum temperature that the payload components would be allowed to experience would be 10°C below the maximum operational temperature of each component in the payload. The thermal model is used to determine what the maximum interface temperature is before the temperature of any of the components violates the 10°C margin of its maximum

operational temperature after a period of operation of the payload. To determine this interface temperature, the temperature boundary conditions of the model, as shown in Figure 3-3, are set to a uniform temperature. The payload is allowed to become isothermalized with the boundary conditions over a sufficient amount of time, and then the heat is dissipated at a rate outlined in Table 3.3, which defines the operation of the payload during a transmission. The uniform temperature of the boundary condition is varied until all components in the model have at least a 10°C margin to their maximum operational temperature at the end of the operation. This method of determining the interface temperature is used because thermodynamically it is the worst case scenario for the payload. While in orbit, the payload will never have the same uniform temperature as the interface temperature due to the dynamic thermal environment in LEO. When the interface reaches that maximum interface temperature, the payload will have to be a lower temperature due to the thermal resistance between the interface and the components that make up the CLICK-A payload. The maximum interface temperature was determined to be 25°C.

For the minimum interface temperature, the minimum operational and survival temperature limits of each component are considered. Ideally, the minimum interface temperature that the interface could become would be 10°C higher than the minimum operational temperature of all the components in the payload. The reason for giving a 10°C margin to the minimum operation temperature is to ensure that the payload will always be able to operate while in orbit. For CLICK-A, that would be the EDFA, which has a minimum operational temperature of 0°C. This would set the minimum interface temperature to 10°C. While this would be ideal, the bus provider thermal engineer recognized that a spacecraft the size of a 3U CubeSat could not maintain an interface temperature range of 10°C to 25°C without the use of an unreasonable amount of heater power in an ISS orbit. The coatings of the spacecraft exterior were chosen to try to limit the temperature fluctuation while on orbit, but since the LEO thermal heating environment can vary significantly, the spacecraft could not maintain that narrow of temperature range without actively heating the interface to the minimum of 10 °C. Due to this limitation, the solution proposed is lowering the

minimum interface temperature to -10 °C during operation. In the absolute worst case cold scenario, which is where the spacecraft is in safe mode and in the coldest orbital scenario, the interface will be allowed to go to -15°C, since the coldest part of the interface will have a heater. Heat is required to maintain this interface temperature if it goes below -15°C, but it is significantly less heater power than needed to maintain the 10°C limit. The -15°C minimum interface temperature provides a 5°C margin to the highest minimum survival temperature for all the components of the payload. As for the minimum interface temperature being -10°C during operation, since the payload will have heaters, it makes sense to allow the temperature of the interface to go below the minimum operational temperature for the EDFA, feedback laser, and TOSA board. The rest of payload should be able to turn on and preheat the components below their operation temperature with the payload heaters.

The bus provider thermal engineer provided expected temperatures of the various faces that enclose the payload for a series of orbits where the payload is off, as well as for one orbit where a transmission happens. For the worst case hot and cold cases, the bus provider thermal engineer modeled the orbit defined in Table 3.5.

Table 3.5: Orbital environment parameters used for worst case hot and cold.

Parameter:	**Hot Case**	**Cold Case**
Altitude	600 km	600 km
Beta Angle	70 Degrees	0 Degrees
Eclipse Duration	0 Minutes	35.5 Minutes
Solar Flux	1420 W/m^2	1300 W/m^2
Earth IR	287 W/m^2	189 W/m^2
Albedo	0.35	0.20

3.5.1 Hot Case

The bus provider thermal engineer supplied the plots in Figures A-1 to A-4 for the temperatures of the faces of the payload-to-bus interface for the worst case hot model. Plots are provided for are a series of orbits where the payload is not operating, as well

as one orbit where the payload is turned on and performs a transmit, with the power draws outlined in Table 3.3. Since the faces of the payload-to-bus interface, labeled in Figure 3-3, are different temperatures, there are two sets of temperatures provided for each group of faces. One group is of faces A, B, C, E, & F due to them being roughly the same temperature. The other group is for face D, which is the interface between the spacecraft chassis and the payload and tends to be warmer than the other faces. Figure A-1 and A-2 show the interface temperature for multiple payload-off orbits, to show how after four orbits the temperature range per orbit becomes the same. The temperatures of the second to last orbit are used to create a nominal payload-off range of temperatures experienced throughout one orbit. Figure A-3 and A-4 show one orbit where the payload is operating, and these payload-on set of temperatures is used to try to align where in time to begin heat dissipation in the model.

The payload-off and payload-on temperature range are combined to create a time series of the temperature of each group of faces over a series of 23 orbits. The temperature vs. time for the boundary conditions for the full 23 orbits modeled is shown in Figure 3-4 for the interface faces A, B, C, E, & F and in Figure 3-5 for the interface face D. The payload is modeled as off for 10 orbits, the transmission begins at the beginning of orbit 11 (at 58,000 seconds), and then an adjusted nominal payload-off temperature range is created for orbit 12 to then begin the payload-off temperature range again for orbits 13-23. The maximum interface temperatures for all faces is 25°C.

3.5.2 Cold Case

The bus provider thermal engineer supplied the plots in Figures A-5 to A-8 for the temperatures of the faces of the payload-to-bus interface for the worst case cold model. As with the worst case hot, the plots are provided for are a series of orbits where the payload is not operating, as well as one orbit where the payload is turned on and performs a transmit, with the power draws outlined in Table 3.3. The same two face groups, as mentioned in Section 3.5.1, are used for the sets of temperatures provided. Figure A-5 and A-6 show the interface temperature for multiple payload-off orbits,

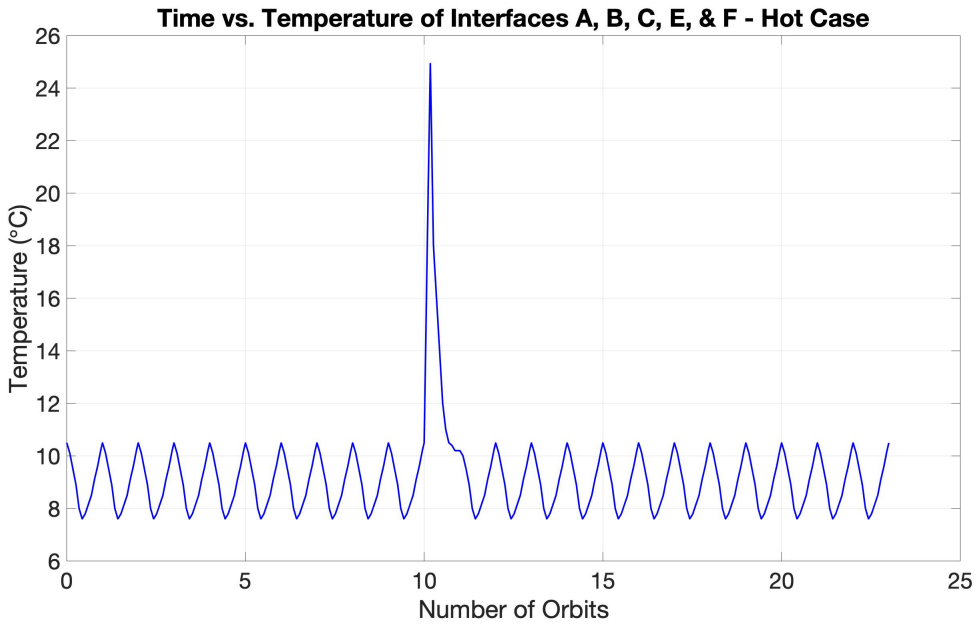

Figure 3-4: Temperature of interface faces A, B, C, E, and F over the entire simulation for worst case hot. The spike in temperature at orbit 11 is when the payload is turned on and a set of transmission heat loads is generated.

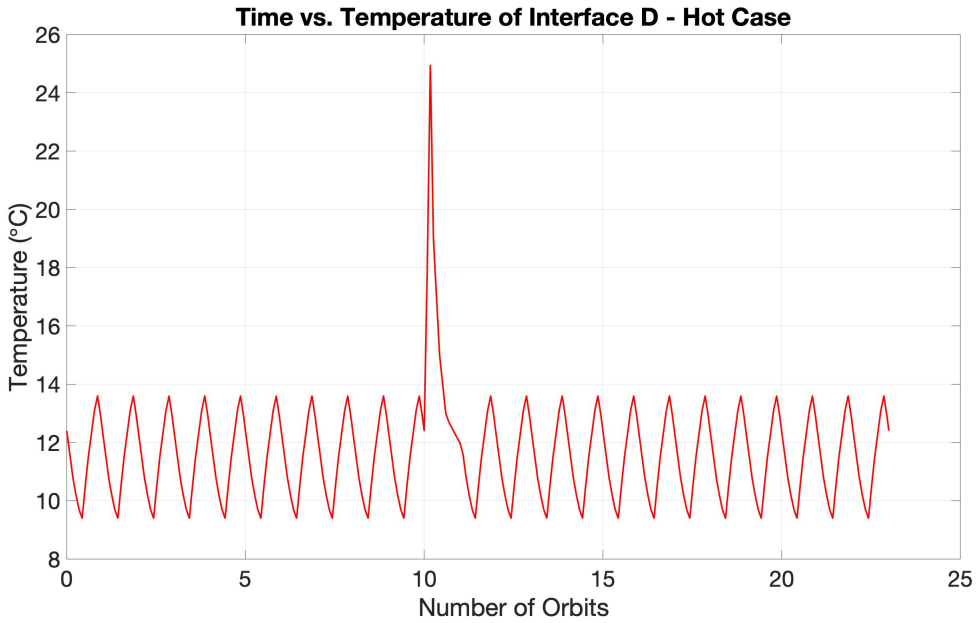

Figure 3-5: Temperature of interface face D over the entire simulation for worst case hot. The spike in temperature at orbit 11 is when the payload is turned on and a set of transmission heat loads is generated.

to show how after four orbits the temperature range per orbit becomes the same. The temperatures of the second to last orbit are used to create a nominal payload-off range of temperatures experienced throughout one orbit. Figure A-7 and A-8 show one orbit where the payload is operating, and these payload-on set of temperatures is used to try to align where in time to begin heat dissipation in the model.

The payload-off and payload-on temperature range are combined to create a time series of the temperature of each group of faces over a series of 23 orbits. The temperature vs. time for the boundary conditions for the full 23 orbits modeled is shown in Figure 3-6 for the interface faces A, B, C, E, & F and in Figure 3-7 for the interface face D. The payload is modeled as off for 10 orbits, the transmission begins at the beginning of orbit 11 (at 54,400 seconds), and then an adjusted nominal payload-off temperature range is created for orbit 12 to then begin the payload-off temperature range again for orbits 13-23. Since the payload-on and payload-off temperature range are pretty much the same, a spike in the interface temperature is not seen in Figures 3-6 or 3-7. The minimum interface temperatures for all faces is -10°C while the payload is operating.

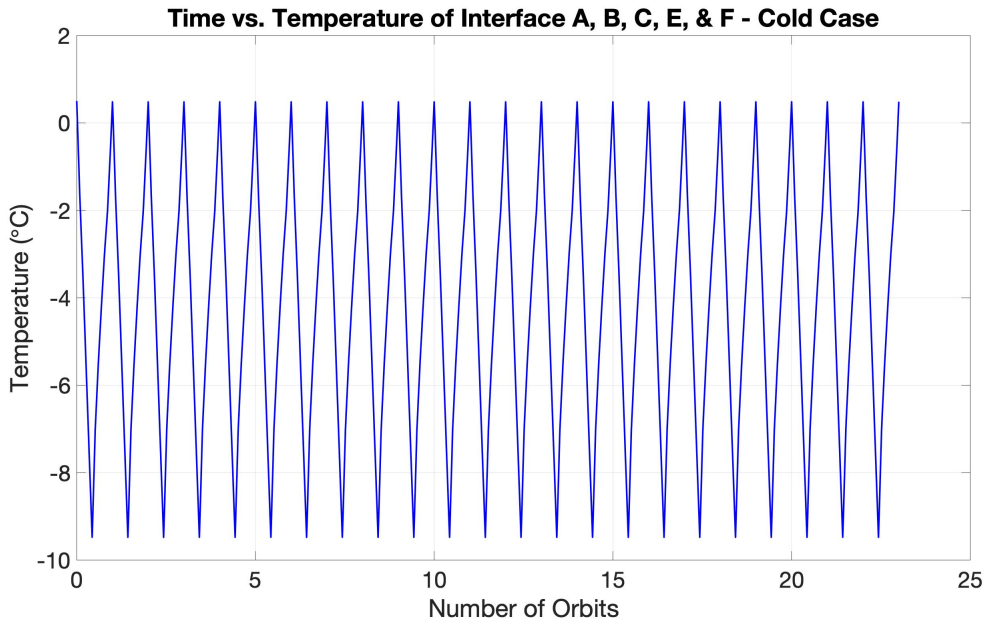

Figure 3-6: Temperature of interface A,B,C,E, and F over the entire simulation for worst case cold.

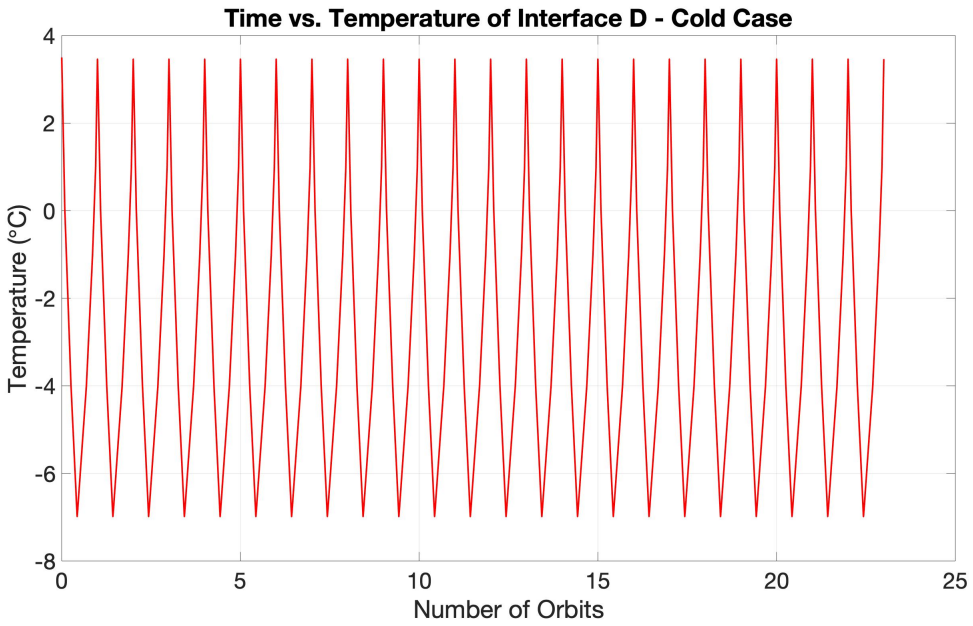

Figure 3-7: Temperature of interface D over the entire simulation for worst case cold.

3.6 CLICK-A Thermal Model

The thermal model for the CLICK-A payload is shown in Figures 3-8 and 3-9 compared to the CAD model. The model is placed inside the boundary condition walls of the bus, shown in Figure 3-3, with temperature defined nodes from Section 3.5.1 and 3.5.2. It can be seen that the complex shapes that are represented in the CAD model are not modeled into the Thermal Desktop model. The exact geometry is not always sought to be represented compared to the correct thermal mass of the object, as noted in Section 3.2.

3.6.1 Results

The CLICK-A model is run in both a worst case hot and worst case cold model scenario. The difference is the transient boundary conditions as described in Sections 3.5.1 and 3.5.2, as well as different starting times of turning on the payload and starting a transmission.

For the hot case, the results are described in terms of the temperature that the components reach through a full set of heat loads defined in Table 3.3 with the

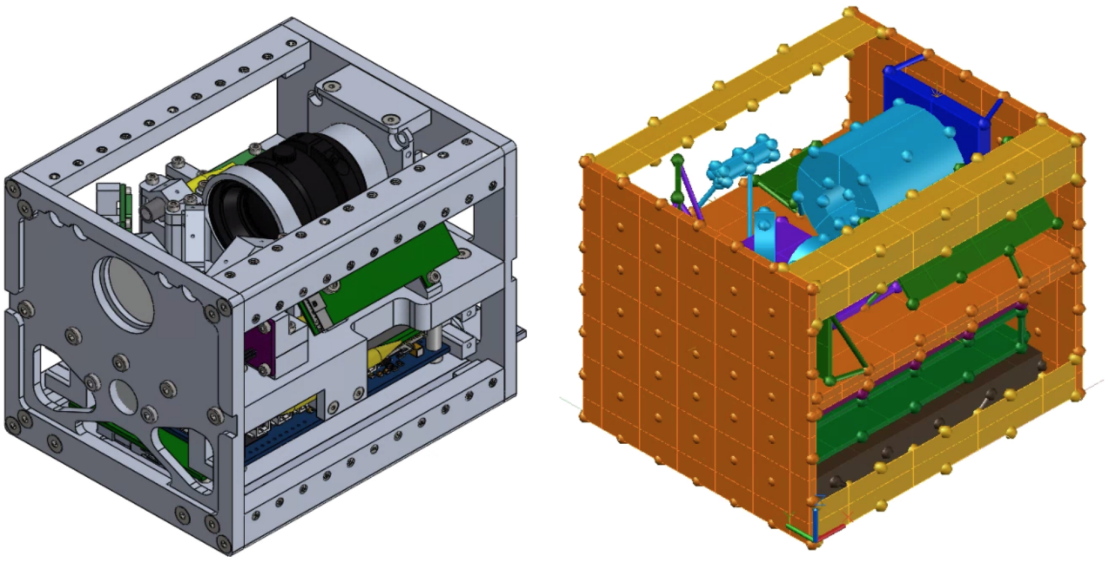

Figure 3-8: CLICK-A CAD V1.4 model compared to the CLICK-A V5 Thermal Desktop model shown in an isometric view.

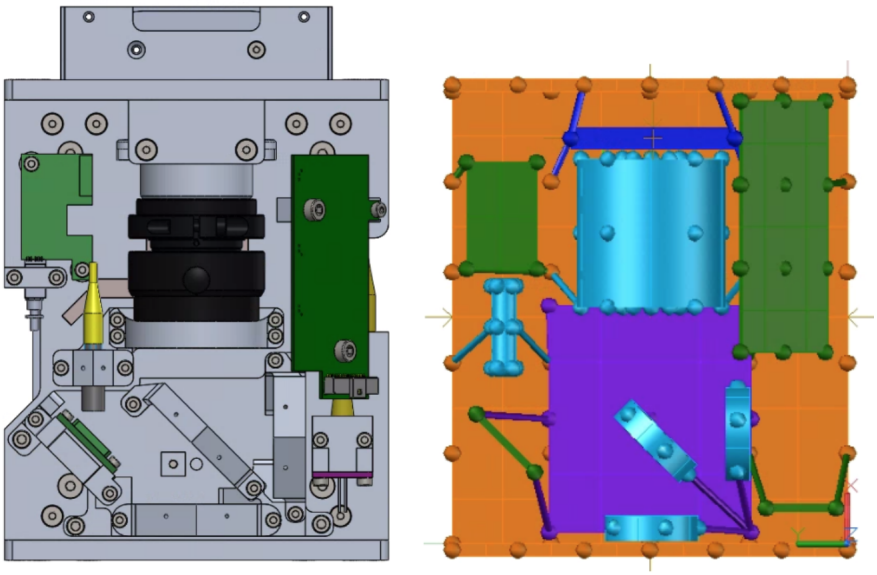

Figure 3-9: CLICK-A CAD V1.4 model compared to the CLICK-A V5 Thermal Desktop model shown in an top-down view.

transient boundary conditions defined in Figures 3-4 and 3-5. These results are shown in Table 3.6.

All the temperatures maintain the 10°C margin to the maximum operational temperature. The components that approach this margin are the components that are the most thermally isolated in the payload and that dissipate a large amount

Table 3.6: CLICK-A thermal model V5 hot case results.

Component	Maximum Survival Temperature (°C)	Maximum Operating Temperature (°C)	Maximum Temperature During Hot Case (°C)	Margin (°C)
TOSA Board	85	75	65	10
Feedback Laser	80	60	36	24
FSM	125	125	33	92
Photodiode Board	85	85	54	31
Beacon Camera	60	45	33	12
EDFA	65	65	34	31
Daughterboard	125	85	66	19
FPGA Board	125	85	73	12
CPU Board	125	85	71	14

of heat during transmission. The FPGA particularly is susceptible to this since its thermal path for conductive cooling is through its standoffs. The Raspberry Pi, called the CPU board, was originally overheating in this model, but a thermal pathway was added between the board and the fiber raceway just below it to dissipate heat away, as described in Section 2.1. The CPU board was the most isolated of all the boards, and since it must be on for the payload to operate, the addition of the gap filler between the main integrated circuit chip on the Raspberry Pi and the fiber raceway allows the heat from the chip to be sunk into the large thermal mass of the fiber raceway.

The cold case is run as a separate version of the CLICK-A Thermal Desktop model, identical to the hot case model, except for the different boundary conditions and the timing of when to turn the payload on. For the cold case, the results are described in terms of the temperature the components are before preheat mode and after the preheat mode with the transient boundary conditions defined in Figures 3-6 and 3-7. The temperatures of the components after a transmission are not included since the none of the components approach their maximum operational temperature. These results are shown in Table 3.7. The asterisk at the bottom of Table 3.7 is denoting which components need to be able to turn on before preheating since those components are the interface with the spacecraft or are used in the heater control. The double asterisk is denoting the components that need to be preheated before operation

since they are below their minimum operational temperature before preheating.

Table 3.7: CLICK-A thermal model V5 cold case results.

Component	Minimum Survival Temperature (°C)	Minimum Operating Temperature (°C)	Minimum Temperature During Cold Case No Heating (°C)	Minimum Temperature During Cold Case After Startup (°C)	Margin (°C)
TOSA Board	-40	-5	-4.2	2.7	7.7
Feedback Laser	-35	0	-4.4	0.5	0.5**
FSM	-40	-40	-4.4	-0.1	39.9
Photodiode Board	-40	-40	-4.3	5	45
Beacon Camera	-40	-40	-4.3	-0.1	39.9
EDFA	-20	0	-4.5	0.5	0.5**
Daughterboard*	-55	-25	-3	8	33
FPGA Board*	-40	-40	-3	22	62
CPU Board*	-55	-40	-3.5	18	58

* Needed for heater functionality ** Does not need to operate for heater functionality

The preheat mode that is shown in Table 3.7 is a 15 minute preheat mode. Originally, a 10 minute preheat was run for the payload, but the feedback laser and the EDFA were not at their operational temperatures yet. A 15 minute preheat mode allows those components to reach their operational temperatures. Further testing will be done during TVAC of the payload to determine the validity of those minimum operational temperatures since, as described in section 2.1.2, the minimum operational temperature stated in a datasheet is not always valid.

The cold case model needed a choice of which heaters to include and where to put them. Both the feedback laser and the EDFA needed to be preheated, and with around 5 Watts of heater power is allotted to the heaters, the choice was which heaters could preheat these components and together add up to around 5 W at 5 Volts. For the EDFA, the choice was between the All Flex Inc. AF-PR3.00-1.50R8P9.00-12.00 and the Birk DK1016-5. The Birk DK1016-5 was chosen since it actually fit on the EDFA and had a reasonable heater output around 3.5 W. This heater is attached to the one of the largest sides of the EDFA, opposite the face that is directly mounted to the payload. While this face is on the cover of the EDFA, it is the only location to fit a large heater. Another heater was added directly to the middle optical plate since the feedback laser is mounted to this plate. The choice for this heater was between

the All Flex Inc. AF-PR1.00-0.50R7P12.50-6.00 and the Birk DK1014-5. The Birk DK1014-5 was chosen since it had a much larger area to spread the heat out compared to the All Flex Inc. AF-PR1.00-0.50R7P12.50-6.00 and still was able to fit under the camera lens.

3.7 CLICK-B/C Thermal Model

The thermal model for the CLICK-B/C payload is shown in Figures 3-10 and 3-11 compared to the CAD model. The model is placed inside the boundary condition walls of the bus, shown in Figure 3-3, with temperature defined nodes from Section 3.5.1 and 3.5.2. Just as with the CLICK-A thermal model, it can be seen that much of the complex shapes that are represented in the CAD model are not modeled in the Thermal Desktop model. The exact geometry is not always sought to be represented compared to the correct thermal mass of the object, as noted in Section 3.2.

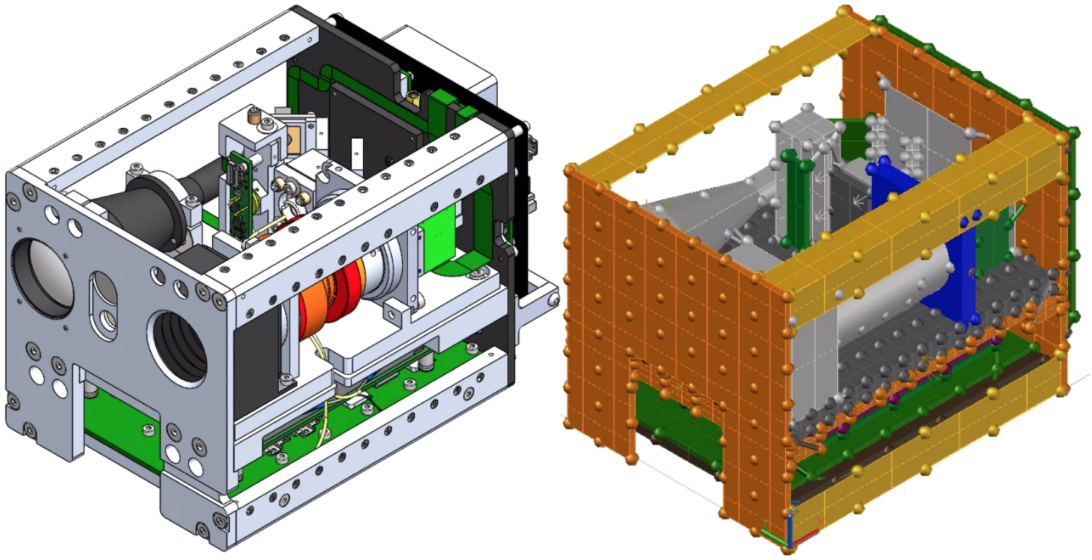

Figure 3-10: CLICK-B/C CAD V1.4 model compared to Thermal Desktop V1 model in isometric view.

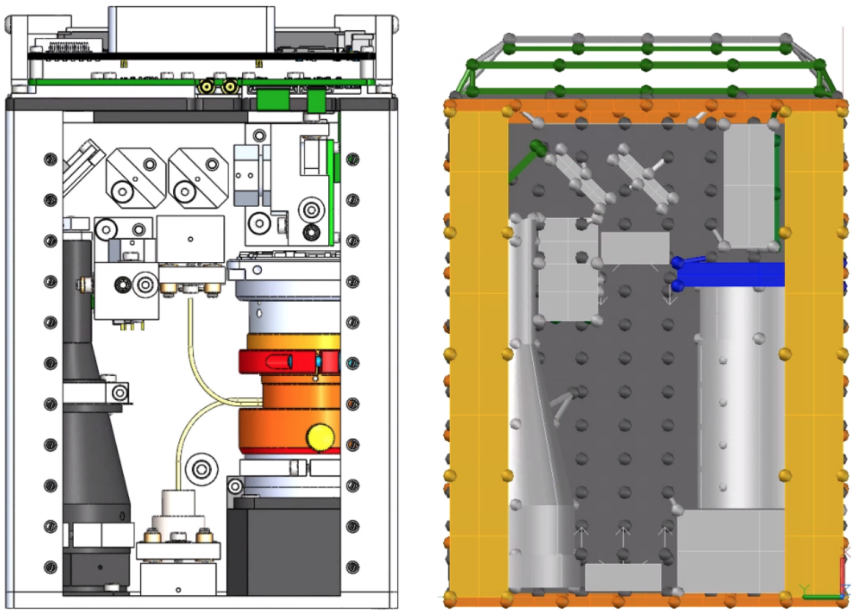

Figure 3-11: CLICK-B/C CAD V1.4 model compared to Thermal Desktop V1 model in top view.

3.7.1 Results

The CLICK-B/C thermal model was run in an identical thermal case scenario as CLICK-A, with a worst case hot and worst case cold. The CLICK-B/C thermal model used the same boundary conditions, described in Sections 3.5.1 and 3.5.2, as CLICK-A since the program is not at a point of identifying different interface temperatures for the CLICK-B/C payloads. The payload heat loads were turned on at the same times as the CLICK-A payload for each case since it is defined by the same model boundary conditions.

For the hot case, the results are described in terms of the temperature that the components reach through a full set of heat loads defined in Table 3.4 with the transient boundary conditions defined in Figures 3-4 and 3-5. These results are shown in Table 3.8.

All the temperatures maintain the 10°C margin to their maximum operational temperature. The large margins can be attributed to two reasons: the choice to use industrialized parts from the outset of the project and the design of the payload being more much conducive to dissipating large heat loads well, as described above Section

Table 3.8: CLICK-B/C thermal model V1 hot case results.

Component	Maximum Survival Temperature (°C)	Maximum Operating Temperature (°C)	Maximum Temperature During Hot Case (°C)	Margin (°C)
Daughter Board	125	85	49.5	35.5
FPGA Board	125	85	62.5	22.5
APD Board	125	85	43	42
CPU Board	85	70	49.5	20.5
Optoelectronics Board	125	85	67	18
Quadcell Board	125	85	25.3	59.7
EDFA	65	65	30.6	34.4
Camera	60	45	25.8	19.2
RPI CM3	80	80	51	29

2.2. The component with the smallest margin predicted during the hot case is the optoelectronics board. This is due to the large heat load that the board is dissipating and lack of definition as to the exact thermal contact between the board and its fiber raceway used to sink heat away. As with the CLICK-A payload, the CPU board was originally overheating in this model. The addition of an aluminum heat spreader plate is required to the back of the Raspberry Pi CM3 module to allow the component to not over heat, as described in Section 2.2.

As with the CLICK-A thermal model, the cold case is also run as a separate version of the CLICK-B/C Thermal Desktop model, identical to the hot case model, except for the different boundary conditions and the timing of when to turn the payload on. For the cold case, the results are described in terms of the temperature the components are before preheat mode and after the preheat mode with the transient boundary conditions defined in Figures 3-6 and 3-7. The temperatures of the components after a transmission are not included since the none of the components approach their maximum operational temperature. These results are shown in Table 3.9. The asterisk at the bottom of Table 3.9 is denoting the components that need to be preheated before operation since they are below their minimum operational temperature before preheating.

The preheat mode that is shown in Table 3.9 is a 10 minute preheat mode. The

Table 3.9: CLICK-B/C thermal model V1 cold case results.

Component	Minimum Survival Temperature (°C)	Minimum Operating Temperature (°C)	Minimum Temperature During Cold Case No Heating (°C)	Minimum Temperature During Cold Case After Startup (°C)	Margin (°C)
Daughter Board	-55	-40	-5.5	1.5	34.5
FPGA Board	-55	-40	-5.5	-2	38
APD Board	-55	-40	-5	-2.8	37.2
CPU Board	-55	-10	-6	-2	4
Optoelectronics Board	-55	-40	-7.5	-6.5	33.5
Quadcell Board	-55	-40	-3.8	-2.8	37.2
EDFA	-20	0	-5	0	0*
Camera	-40	-40	-3.7	-2.6	37.4
RPI CM3	-25	-25	-5.5	3	19.5

*Commanded to this temperature for heater set point

EDFA has a heater attached to it that is set to preheat it to 0°C, which explains the lack of margin for that component. The heaters modeled for the cold case showed that a heater power of 6.5W is needed to meet the required 0°C minimum operating temperature of the EDFA during a 10 minute preheat. The heaters that need to be attached to the EDFA have not been chosen for the CLICK-B/C payloads yet, but some combination of the heaters outlined in Table 2.2 will be chosen by the thermal engineer and electrical engineers for the project. As for the CPU board, the current thermal design does not maintain the 10°C margin that is ideal for components. Given that these margins are based on the boundary conditions for the CLICK-A payload, it will be suggested that the interface temperatures for the CLICK-B/C payload be raised by around 5°C to allow the CPU to maintain the 10°C margin to its minimum operating temperature and relax the heater requirements for the EDFA.

3.8 Thermal Model Summary

The thermal design that was discussed in Chapter 2 was implemented in thermal models for the CLICK-A payload and the CLICK-B/C payloads. The CLICK-A components that did not use heaters all met the 10°C margin for their maximum and minimum operational temperature. The CLICK-A components with heaters were

shown to preheat in 15 minutes and reach their minimum operational temperature. The CLICK-B/C components that did not use heaters almost all met the 10°C margin for their maximum and minimum operational temperature, but has motivated an increased in the interface temperature by 5°C between the spacecraft and payload for CLICK-B/C compared to CLICK-A. The CLICK-B/C components with heaters were shown to preheat in 10 minutes and reach their minimum operational temperature. The next Chapter will discuss the development of the thermoelastic model and how the CLICK-B/C thermal model was used to calculate the thermoelastic misalignment of the payload during operation.

Chapter 4

Thermoelastic Model Development and Results

Thermoelastic modeling is an analysis that calculates how the change in temperature of a material creates a strain due to its coefficient of thermal expansion, which imparts dimensional and positional changes in optics and their mounts [37]. For the CLICK project, this type of analysis is relevant to the fine pointing error budget of the payloads [38]. Since the optical communication link relies upon the transmitter's ability to point its laser, each link has a fine pointing analysis performed to predict the ability for the laser to be pointed correctly. This fine pointing analysis accounts for many aspects that affect the pointing of the payload [38]. This chapter focuses on the thermoelastic deformation of certain optical mounts and how those deformations create a misalignment of the optics.

The thermoelastic analysis outlined in this chapter does not need to be performed for the CLICK-A payload for two reasons. First, the CLICK-A mission utilizes a calibration laser, as mentioned in Section 1.3.1, which is able to determine the where the transmitting laser source is in reference to the received beacon [23]. Due to this calibration laser, the payload is able to sense almost all thermoelastic deformations and correct for them with the FSM. Second, the thermoelastic deformations that cannot be corrected for are estimated to be two orders of magnitude less than other misalignment sources in the payload. This was first estimated in Derek Barnes mas-

ters thesis [26], but the current estimate is located in the Peter Grenfell's CLICK-A pointing budget [39].

4.1 CLICK-B/C Thermoelastic Model Development

This section describes the process of developing the thermoelastic model and explains how the work in the previous Chapter supports this analysis. There are many ways to perform thermoelastic analysis, depending on the degree of complexity one chooses to undertake in the model. One form of optomechanical deformation analysis is called structural-thermal-optical performance modeling, referred to as STOP modeling [37]. The analysis performed in this section does not include optical performance, but does calculate the relative angular deformation of the optical mounts with respect to their aligned positions. The overall misalignment of the transmit and receive beam is calculated using these optical mount angular deformations. If the results of this analysis show the misalignment of the mounts of the optics to be well beyond what is reasonable with respect to the pointing analysis, then further STOP modeling can be pursued to determine how the deformation is impacting the optical performance of the payload.

For the CLICK-B/C payloads, the thermoelastic analysis performed is used to determine how the optical component mount deformations cause misalignment of certain optical components. This is important due to the fact that the CLICK-B/C payload does not utilize a calibration laser. The misalignments due to the optical component mount deformations are not detectable on orbit by the payload and create an angular error in the pointing of the payload. The misalignment for thermoelastic distortions is budgeted in the fine pointing budget 5.396 μrad. Other sources of misalignment are the transmit collimator to quadrant photodiode alignment, with 9.178 μrad budgeted, and FSM control residual, with 3.077 μrad budgeted. The total of the pointing error terms accounted for in the pointing budgeted is 20.863 μrad [38]. The optical mounts that are primarily affected are shown in Figure 4-1 and include the transmit collimator mount, dichroic 2 mount, dichroic 1 mount, and the quadrant

photodiode mount. These components are aligned in the lab and are not able to be adjusted on orbit.

There are two primary angular deformations that this analysis is investigating. First, the deformation of the transmit collimator mount with respect to the mount that holds the dichroic that is used to reflect the light from the transmit collimator, labeled dichroic 2 in Figure 4-1. The deformation of these mounts with respect to each other creates an angular misalignment of the transmitted beam. The second deformation that this analysis is calculating is the deformation of the mount for the dichroic used to reflect the beacon wavelength, labeled dichroic 1 in Figure 4-1, and the quadrant photodiode mount with respect to each other. Since the FSM is a controllable element of the optical train, the misalignment of these mounts will be detected by the quadrant photodiode sensor and corrected. The algorithm controlling the FSM position is based on where the beam falls on the quadrant photodiode, this misalignment will be corrected by adjusting the angle of the FSM. This adjustment will create an angular error of the alignment of the transmit path to the receive path and create an angular offset of the transmit beam out of the payload. Figure 4-2 shows an what an exaggerated misalignment between the receive and transmit beams would look like.

There have been previous efforts within the CLICK project to understand how the thermoelastic deformations cause misalignment of the optics. One was performed by Michael Long in his masters thesis [40]. Long's previous effort was of an earlier version of the payload design, and used uniform increases in the temperature of the payload as well as thermal gradients across the payload optical bench to analyze deformations. The outputs of Long's analysis were rigid body displacements and tip/tilt of optical components with respect to each other. These outputs were fed into into an optical model software called Zemax to calculate how the optical components' movement impacted the optical performance of the payload. Since the payload has changed quite significantly, these deformations are no longer up to date. Another effort undertaken by Laura Yenchesky involved analysis of the thermal deformation of a 3U satellite bus in orbit, like the one used for the CLICK payloads. This aspect

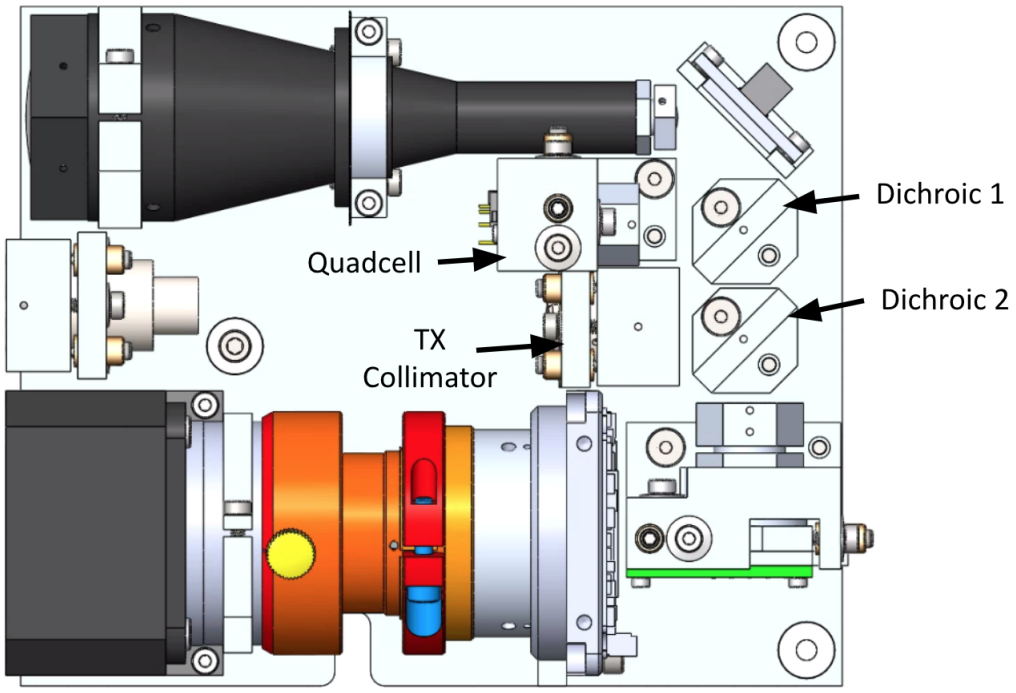

Figure 4-1: Optical components who deformations are calculated in the thermoelastic analysis of the optical bench from CLICK-B/C CAD V1.4 model.

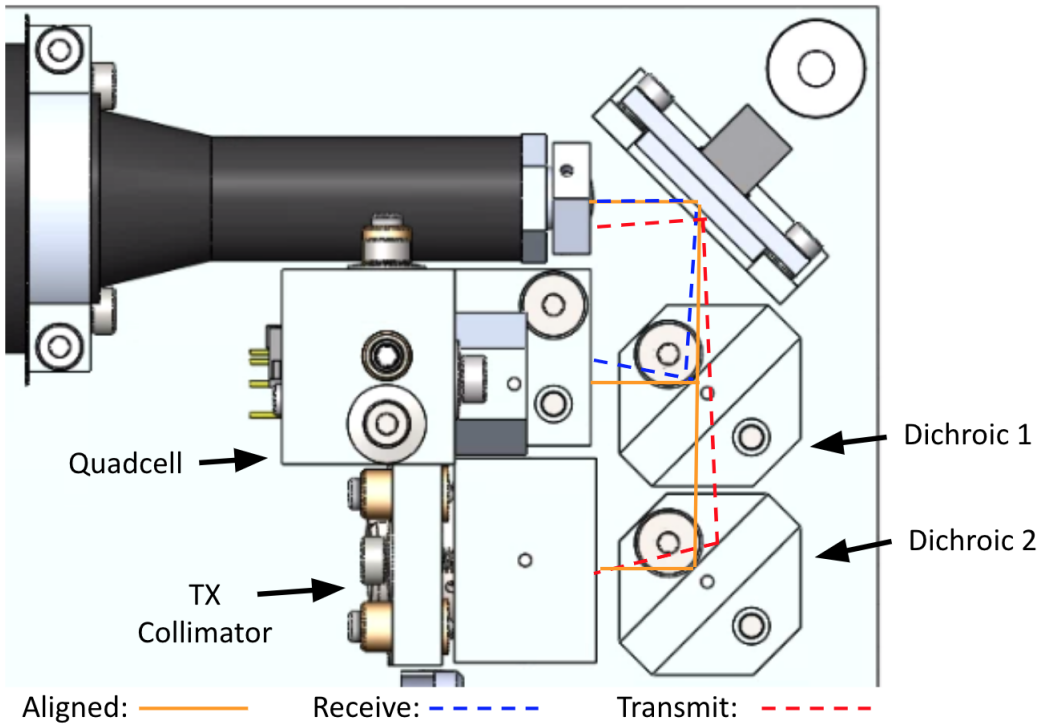

Figure 4-2: Exaggerated misalignment depiction that could be caused by thermoelastic shifting of the analyzed optical components. Optical bench from CLICK-B/C CAD V1.4 model.

also affects the pointing of the laser and was characterized in her undergraduate thesis [41].

4.1.1 Thermal Model Refinement

To create a thermoelastic model, one needs to apply temperatures to a structural model to see how those temperatures deform the structure [37]. For the structural model created in this analysis, the temperatures are mapped from a Thermal Desktop model of the payload. As discussed in Chapter 3, Thermal Desktop primarily uses finite difference surfaces and solids to represent components in a thermal model. When higher fidelity is needed, Thermal Desktop allows the use of finite element meshes. These finite element meshes allow for a closer representation of the actual part being modeled, but usually require many more nodes to represent the same thermal mass as a finite difference solid.

To create a more accurate representation of the CLICK-B/C optical bench in Thermal Desktop, the SolidWorks file of the optical bench was simplified to reduce features, such as extraneous holes and fillets, that tend to create large meshes in a finite element meshing software. This simplified optical bench was imported into FEMAP to use its finite element meshing capabilities. The process of creating the simplified optical bench model and thermal mesh from the original optical bench model is shown in Figure 4-3. The coarse finite element mesh was created and exported as a FEMAP neutral file. This neutral file, which contains the nodes and elements of the simplified optical bench model, was imported into into the Thermal Desktop CLICK-B/C model, who results are described in Section 3.7. The original thermal model of the CLICK-B/C payload had a simple aluminum plate to represent optical bench, which was too coarse to use to map temperatures to a more detailed model such as the one used in the thermoelastic structural model. The new optical bench representation in the Thermal Desktop model had its thermal connections rebuild to conduct heat like the original simple aluminum plate. The original thermal model of the CLICK-B/C is built in Thermal Desktop 5.7 and the payload used 1496 nodes and could be run in under a minute. The new model, also built in Thermal Desktop

5.7 and with the new refined optical bench model finite element mesh, had 3324 nodes and took around 30 minutes to solve. The new model has its component temperatures compared to the simplified optical bench model and it is observed that the two models report the same results. The finite element optical bench temperatures, as well as temperatures of the dichroic and quadrant photodiode mounts, were exported using text files that enumerated their node number, location, and temperature.

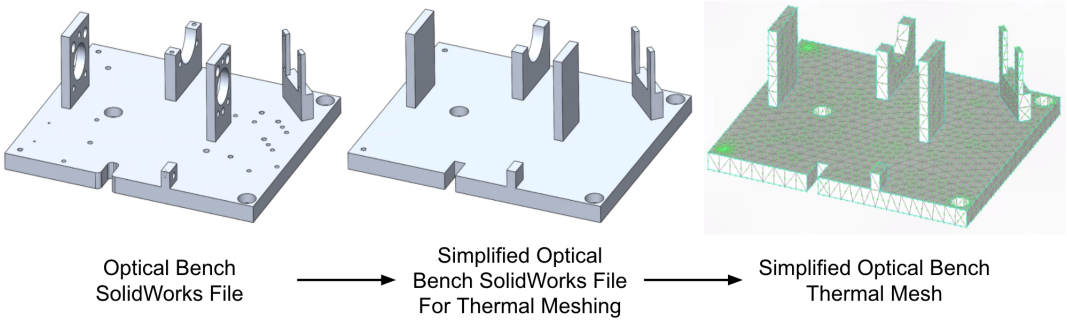

Figure 4-3: Process of creating a simplified optical bench thermal mesh from the original optical bench SolidWorks file from CAD model V1.4.

4.1.2 Structural Model Development

The thermoelastic model produces a set of X, Y, and Z translations of each of the nodes, which comprise the mesh, of the structural model that the thermal model temperatures are mapped to. As with the thermal mesh, the structural model meshing process required the creation of a simplified optical bench model. This structural model could have much more refinement in its mesh to allow higher fidelity of the model, due to the numerical simplicity of running a static stress analysis with a finite element model compared to the transient thermal model with a combined finite difference and finite element mesh that runs over 1,300 time steps. The same simplification is performed for this model as was performed for the simplified thermal mesh. The process of creating the simplified optical bench model and structural mesh from the original optical bench model is shown in Figure 4-4.

To simplify the development of the structural model, both the dichroic mounts and quadrant photodiode mount are modeled to be part of the simplified optical bench

model. The structural modeling software will treat the imported simplified optical bench model as one homogeneous piece of aluminum. This simplification is made due to the manner in which these mounts are fastened to the optical bench. Since the mounts are fastened with a countersunk bolt and a grouted pin to the bench, the mounts should deform much the same as a homogeneous piece of aluminum would. This optical bench was given the material properties of Aluminum 6061-T6. The telescope as well as the beacon camera and lens were not included in the structural model to simplify modeling. The mounting of these components and where they are located on the optical bench means the addition of these components would have little impact on the deformations experienced by the specific optical mounts being analyzed. Also, these components are mounted off the surface of the optical bench and have a well defined thermal path so they should make the optical bench more rigid, as well as expand and contract with the optical bench.

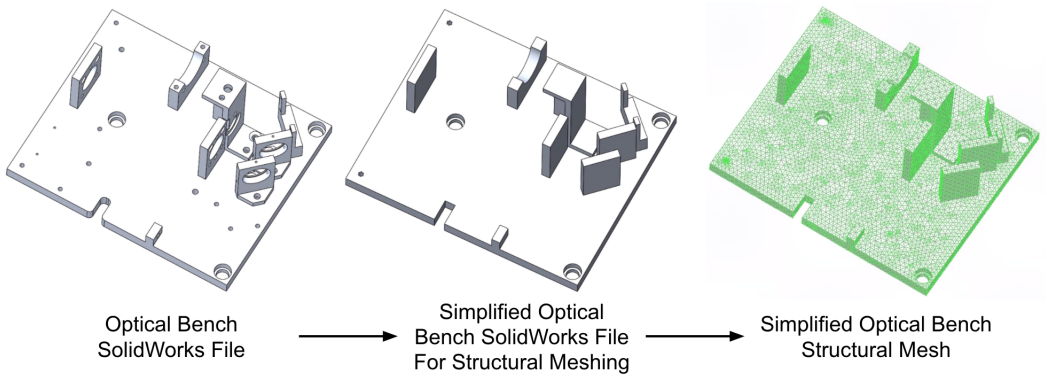

Figure 4-4: Process of creating a simplified optical bench structural mesh from the original optical bench SolidWorks file from CAD model V1.4. The reader is directed to notice the difference in mesh density between the thermal mesh and the structural mesh.

Another critically important aspect of the structural model used in thermoelastic modeling are the boundary conditions that are applied to the mesh. For the thermoelastic structural model, the boundary conditions imposed on the optical bench structural mesh need to reflect how the optical bench is mounted inside the payload. The optical bench is separated from the middle structural plate, called the EDFA plate, with titanium spacers. A picture of how these titanium spacers interface with

the both the optical bench and the EDFA plate is shown in Figure 4-5. The titanium spacers fit in a hole in both the optical bench and a hole in the EDFA plate. These spacers have a 0.001 inch tolerance between the spacer and the holes for the spacer. This tight tolerance limits the launch load induced shift that could occur between the payload structure and the optical bench. The tight tolerance between these components also has implications on how the boundary conditions of the structural model should be modeled. Since these components are designed with very little ability to shift, that means that the optical bench is essentially fixed at these locations by the titanium spacers. Due to this, the nodes that are in contact with the titanium spacers are set to "fixed" in the FEMAP structural model. The locations of the fixed nodes, highlighted in blue, is shown in Figure 4-6.

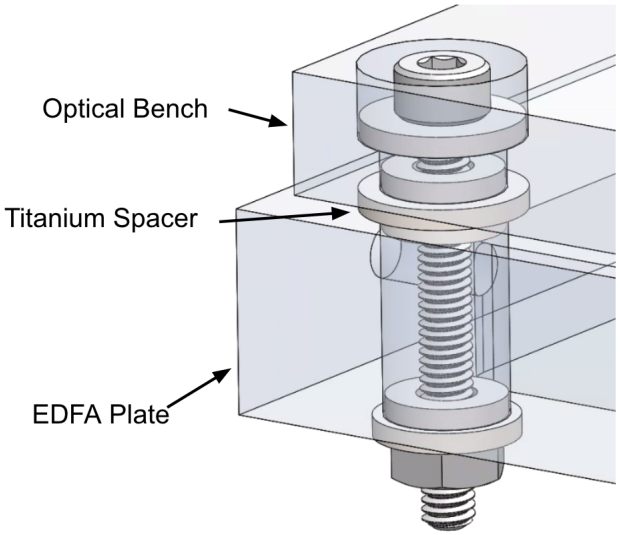

Figure 4-5: Titanium spacers used to thermally isolate the optical bench as well as locate it with respect to the EDFA plate. Picture from CLICK-B/C CAD model V1.4.

4.1.3 Mapping Thermal Results to Structural Model

To perform the thermoelastic analysis of the optical bench and its mounts, the temperatures of the thermal model need to be mapped to the structural model [37]. The simplest form of mapping is to take the location of each node of the structural mesh and calculate which node of the thermal model is closest. The thermal node that

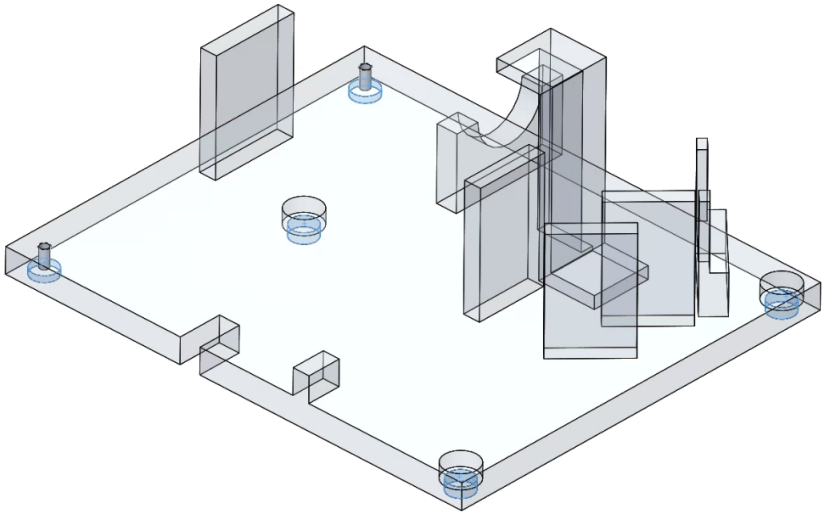

Figure 4-6: Location of the areas with fixed nodes on the optical bench are highlighted in blue. Picture from CLICK-B/C CAD model V1.4.

is closest the structural node being evaluated has that thermal node temperature assigned to it [37]. Equation 4.1 is used to calculate the distance, D, between the structural and thermal nodes. The X_{FEMAP}, Y_{FEMAP}, and Z_{FEMAP} terms define the location of the FEMAP structural node and the X_{TD}, Y_{TD}, and Z_{TD} terms define the location of the Thermal Desktop thermal node.

$$D = \sqrt{(X_{TD} - X_{FEMAP})^2 + (Y_{TD} - Y_{FEMAP})^2 + (Z_{TD} - Z_{FEMAP})^2} \tag{4.1}$$

For each structural node, a distance is calculated between that node and every thermal node. These distances are saved and thermal node with the minimum distance has its temperature assigned to the structural node number being evaluated. For the structural model with 113,072 nodes and a thermal model with 2,194 nodes, this mapping process can take quite a while. As long as neither mesh changes, the mapped thermal nodes to structural nodes list can be used for whatever thermal results need to be evaluated using the structural model.

4.1.4 Determining Cases to Analyze

The thermal model, as described in Sections 3.5.1 and 3.5.2, runs a worst case hot and worst case cold simulation which represent the maximum and minimum temperatures that the payload will experience in orbit. For each of these cases, there are many orbits modeled, but only one orbit where a transmission occurs. For the orbit where the payload is transmitting, that is the relevant time for the thermoelastic analysis.

The goal is to determine what the maximum deformation would be for the optical mounts for each case. The instance in time during the transmission that represents the worst case temperature distribution is selected. For the hot case, this is at the end of the transmission, when the difference in temperature across the optical bench was maximum. This time is also the time when the difference in temperature between optical bench and the EDFA plate is largest. For the cold case, the instance in time that had temperatures mapped also corresponded to the end of the transmission, when the difference in temperature between optical bench and the EDFA plate is largest. The results of the cases and their impacts are described in Section 4.2.

4.1.5 Pointing Error Calculation

The thermoelastic model produces a set of X, Y, and Z translations of each of the nodes of the structural model that the thermal model temperatures are mapped to. To determine how these deformations will affect the pointing of the payload, the deformations are exported from FEMAP and imported into MATLAB. As discussed in the beginning of this chapter, the components that are of interest in this analysis are the transmit collimator mount, the two dichroic mounts, and the quadrant photodiode mount.

Since this analysis calculates how these mounts are deforming relative to each other, a technique is developed to fit a plane to the nodes that comprise a certain face each of the mounts. The technique uses linear regression type of plane fitting where a system of linear equations is solved to define the equation of the best fit plane for the face of the mount. The faces chosen to define the planes that evaluate the

angular deformation of the mounts is shown in Figure 4-7. It should be stated that the mounts do not perfectly maintain planarity while deforming, but the deformation from planarity was seen to be an order of magnitude less than the whole mount deformation, so it was determined that treating the mount as planar would be a good approximation. A coefficient of determination was calculated to show how well the plane equation fits to the FEMAP deformation data for each mount. The coefficient of determination was calculated to be 0.995 or greater for all the planes fit for the cases analyzed.

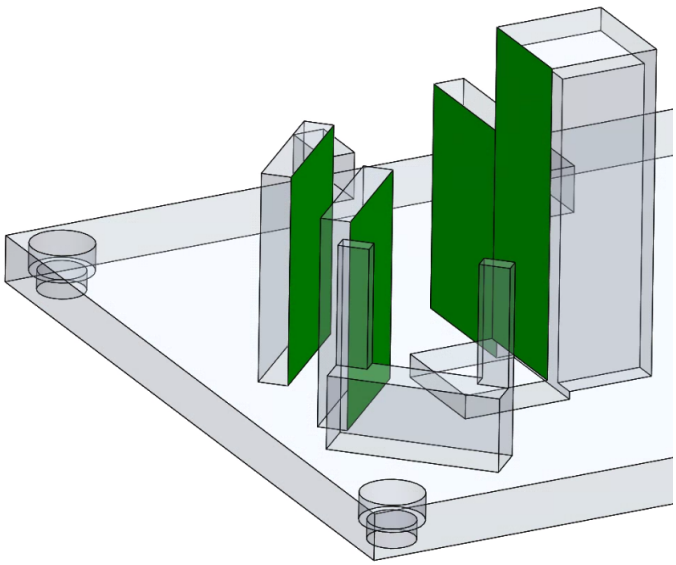

Figure 4-7: Location of the faces that are used to evaluate the angular deformation of the optical mounts. Picture from CLICK-B/C CAD model V1.4.

The planes of best fit for each mount were used in a specular reflection analysis to see how the transmit and receive pointing was angularly perturbed. The equation that defines the law of reflection is shown in Equation 4.2 [42]. The v term is a vector that defines the direction the ray is traveling before being reflected, the n term is a vector that defines the normal of the plane that is reflecting the ray, and the v' term is the reflected ray vector. This equation is used to calculate the vector of the light leaving a reflected surface given the vector of the light before hitting the mirror and the normal to the plane that is reflecting the ray [42].

$$v' = v - [2v \cdot n]n \tag{4.2}$$

The angular deformation is calculated for both the transmit and receive paths. For the transmit path, the normal of the transmit collimator mount plane is used as the vector to represent the ray being transmitted by the transmit collimator, the v term in Equation 4.2. The normal of the plane that defines the dichroic 2 mount is used as the n term in Equation 4.2 since the dichroic 2 mount holds an optic that reflects almost all the transmitted light. The vector of the light that reflects off the dichroic 2 plane is calculated for both the undeformed and deformed mounts. The angular difference in these vectors is calculated with Equation 4.3 [42] that uses determines the angle between the two vectors. The undeformed vector is the v_1 and the v_2 is the deformed vector in Equation 4.3.

$$cos(\theta) = \frac{v_1 \cdot v_2}{|v_1||v_2|} \tag{4.3}$$

The receive path is a bit more complicated because it is not a transmitting path. To determine the angular deformation that is occurring with the optical component mounts that define the receive path, the quadrant photodiode is treated as a transmitting source, with the normal of the quadrant photodiode mount defined as the v term in Equation 4.2. The reason the quadrant photodiode mount is treated as a transmitting source is to capture its deflection in the ray reflection calculation. Due to the fact that the quadrant photodiode sensor will be mounted parallel to the face of the mount being evaluated, as the quadrant photodiode sensor moves when the mount deforms, the angle that the FSM needs to correct for to center the receive beam on the center of the sensor is equivalent to the angle that the mount is deforming. The reflecting surface for this path is the dichroic 1 mount. The vector of the light that reflects off dichroic 1 is calculated for both the undeformed and deformed mounts. The angular difference in these vectors is calculated with Equation 4.3 [43] just as with the transmitting calculation.

The two misalignment angles for the transmit and receive paths are calculated for

the deformations that occur within the payload. For the transmit path, the change in the angle of the beam leaving the payload is the transmit misalignment angle divided by the telescope magnification, which is 10.5. For the receive path, the change in the angle of the beam leaving the payload is also its misalignment angle divided by the telescope magnification. The reason the receive path is also divided by the telescope magnification is because the deformations of the optical mounts of the receive path will cause the FSM to need to correct for those angular deformations and require the FSM to change its angle to center the beam on the quadrant photodiode. The angle that the FSM corrects for will change the angle of the transmitting beam, and since this beam is transmitted through the telescope, the impact of the receive misalignment on the beam leaving the payload is reduced by the telescope magnification. The root sum square of the two misalignment angles is calculated since that is often how pointing errors are analyzed in a pointing budget [38]. The root sum square value of the pointing error induced because of thermoelastic deformations is what is fed into the fine pointing budget to determine its impact on pointing [38]. The reader is referred to Grenfell [38] for discussion on the fine pointing budget and all the terms included in the analysis.

4.2 CLICK-B/C Thermoelastic Model Results

The CLICK-B/C thermoelastic model is run for both the worst case hot and worst case cold model instances in time. It was observed that the increased temperature of the EDFA plate compared to the optical bench was the primary driver of the thermoelastic distortions. This is due to the EDFA plate expanding more than the optical bench and the thermal isolators constraining the mounting points of the optical bench rigidly. As the optical bench is cooler, it does not expand as much as the EDFA plate and the thermal isolators between the optical bench and EDFA plate cause deformations in the optical bench. It is observed that the larger the difference in temperature between the optical bench and the EDFA plate, the larger the deformations. The misalignment that is calculated for the current thermal design of the optical bench

is double what the fine pointing budget had budgeted for thermoelastic error. Originally, as described in Section 2.2.2, the optical bench was designed to be thermally isolated from the EDFA plate to reduce the thermal gradients across it and limit the thermoelastic deformations. The titanium spacers in between the optical bench and the EDFA plate serve as thermal isolators, but also rigidly affix the optical bench to the EDFA plate. The rigidity of this connection is what allows the optical bench to be deformed by the difference in temperature between the optical bench and the EDFA plate. The difference in temperature between the two plates was not originally considered in the design.

There are two different types of solutions that could solve the issue of the optical bench deforming in the manner described above. The first solution, which is implemented in this analysis, is to keep the optical bench mounting the same and thermally couple the optical bench to the EDFA plate to decrease the difference in temperature between the two parts. The easiest way to implement this solution is to minimize the gap in between the optical bench and EDFA plate and add thermal gap filler material between the two. The second solution is to design a mounting flexure between the optical bench and the EDFA plate. The flexure would allow there to be a larger difference in temperature between the optical bench and the EDFA plate since the flexure would be designed to flex predictably as the two components changed dimensions with temperature. The second solution was out of the scope of this analysis since it requires considerable mechanical design alterations. The program will need to investigate the implications on the optical performance of the payload for the first solution to ensure that this design choice is the best path forward to reduce thermoelastic misalignment. This is due to the larger range of temperatures that the optics will experience not being thermally isolated.

Described in Sections 4.2.1 and 4.2.2 are the thermoelastic deformation results of having the optical bench thermally isolated from the EDFA plate, as well as the results when the two are thermally coupled.

4.2.1 Hot Case

The results shown are for both the thermally isolated and thermally coupled optical bench at the instance in time of 59,500 seconds in the hot case thermal model. As mentioned in Section 4.2, the model with an optical bench that is thermally isolated creates a thermoelastic misalignment that is double what the fine pointing budget has budgeted for thermoelastic error. The thermoelastic misalignment is 10.48 μrad for the thermally isolated optical bench. An increase of the conductance between the optical bench and the EDFA plate was added to mitigate this, and the process of generating thermoelastic results is repeated. The increase in conductance reduced the temperature difference between the EDFA plate and the optical bench from 4.1°C to 0.3°C. The MATLAB representation of the deformed optical mount planes, as seen in Figure 4-7, are shown in Figure 4-8a for the hot thermally isolated case and Figure 4-8b for the hot thermally coupled case. The results of each of the models is shown in Table 4.1. It can be seen that the increase in thermal conductance between the optical bench and the EDFA plate helped to reduce the thermoelastic misalignment by a factor of 2.17, from 10.48 μrad to 4.82 μrad. The thermally coupled optical bench thermoelastic misalignment is below the budgeted 5.396 μrad.

4.2.2 Cold Case

As with the hot case, the results shown are for both the thermally isolated and thermal coupled optical bench. The instance of time that was chosen for thermoelastic analysis was 55,900 seconds. The cold case model with an optical bench that is thermally isolated creates a thermoelastic misalignment of 7.59 μrad, which is still significantly higher than the 5.396 μrad that the fine pointing budget had budgeted for thermoelastic error. The same process of updating the model to increase the conductance between the optical bench and the EDFA plate is added to mitigate this, and the process of generating thermoelastic results is repeated. The increase in conductance reduced the temperature difference between the EDFA plate and the optical bench from 2.5°C to 0.25°C. The MATLAB representation of the deformed

optical mount planes, as seen in Figure 4-7, are shown in Figure 4-9a for the cold thermally isolated case and Figure 4-9b for the cold thermally coupled case. The results of the each of the models is shown in Table 4.2. It can be seen that the increase in thermal conductance between the optical bench and the EDFA plate helped to reduce the thermoelastic misalignment by a factor of 1.85, from 7.59 μrad to 4.11 μrad. The thermally coupled optical bench thermoelastic misalignment is below the budgeted 5.396 μrad.

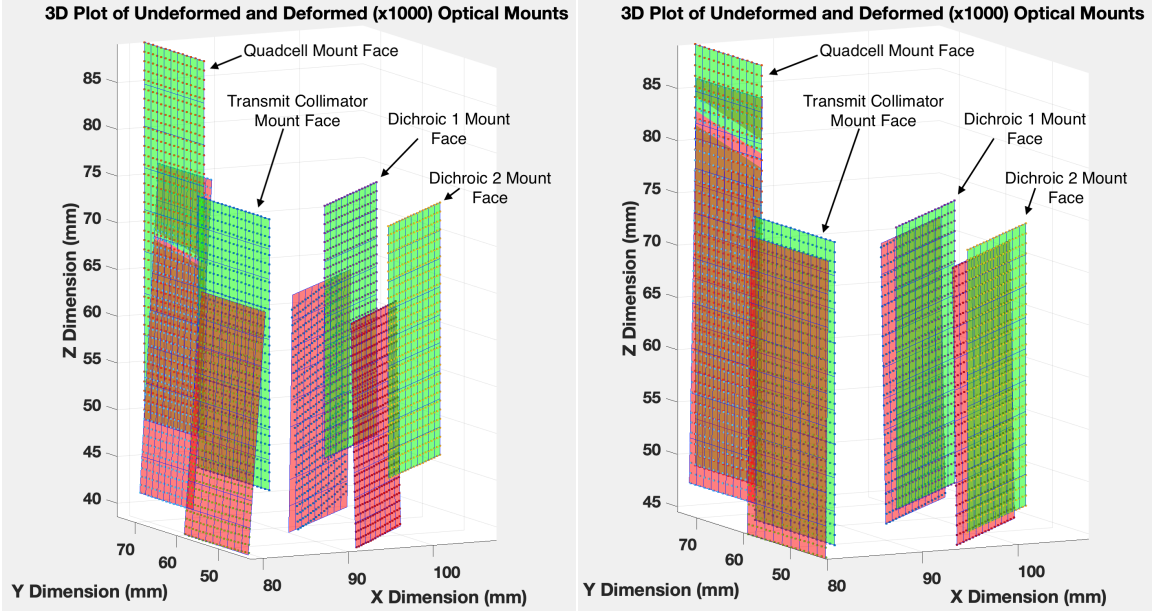

(a) Isolated from EDFA plate.

(b) Coupled to EDFA plate.

Figure 4-8: 3D plot of undeformed (green) and deformed (red) nodes and fitted planes for optical mount faces. The deformations have been multiplied by 1000 to make it easier to see the deformations. Results are from hot case models of the V1 thermoelastic FEMAP model.

Table 4.1: Results of hot case CLICK-B/C thermoelastic analysis.

Case	**Isolated Optical Bench Results**	**Coupled Optical Bench Results**
Transmit Collimator Deformation (μrad)	69.37	10.73
Dichroic 2 Deformation (μrad)	21.29	13.19
Dichroic 1 Deformation (μrad)	15.83	14.44
Quadcell Deformation (μrad)	55.17	19.72
Transmit Path Deformation (μrad)	96.72	29.69
Receive Path Deformation (μrad)	52.49	40.93
Telescope Magnification	10.5	10.5
Root Sum Square of TX and RX Deformation (μrad)	10.48	4.82
Budgeted Error (μrad)	5.396	5.396

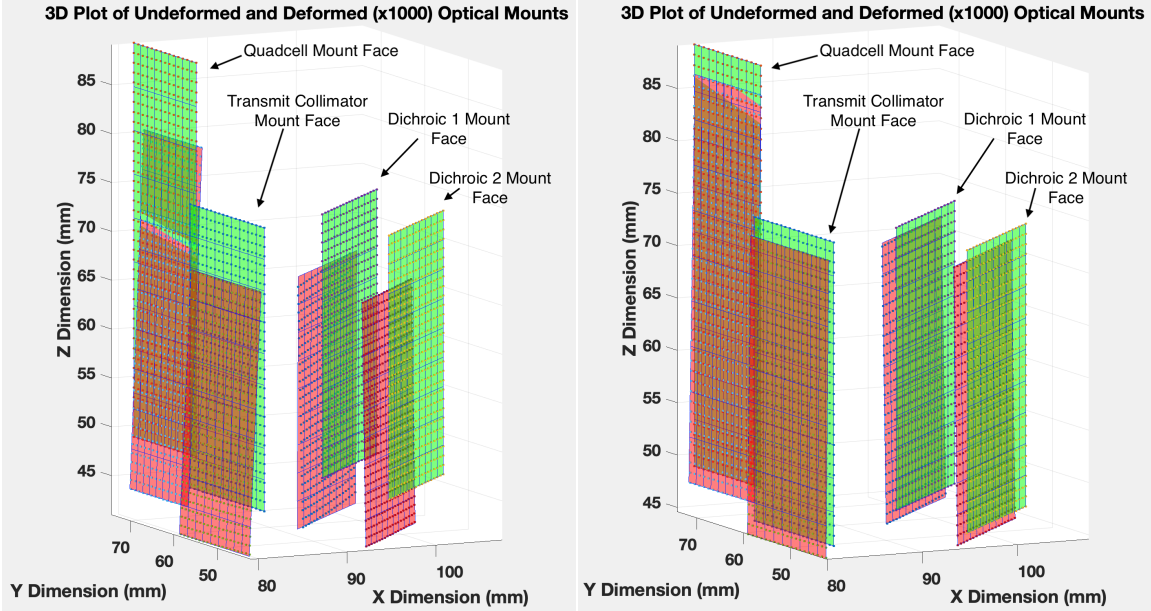

(a) Isolated from EDFA plate.

(b) Coupled to EDFA plate.

Figure 4-9: 3D plot of undeformed (green) and deformed (red) nodes and fitted planes for optical mount faces. The deformations have been multiplied by 1000 to make it easier to see the deformations. Results are from cold case models of the V1 thermoelastic FEMAP model.

Table 4.2: Results of cold case CLICK-B/C thermoelastic analysis.

Case	**Isolated Optical Bench Results**	**Coupled Optical Bench Results**
Transmit Collimator Deformation (μrad)	45.88	9.97
Dichroic 2 Deformation (μrad)	16.56	11.39
Dichroic 1 Deformation (μrad)	8.78	12.19
Quadcell Deformation (μrad)	39.87	16.18
Transmit Path Deformation (μrad)	67.85	26.41
Receive Path Deformation (μrad)	41.85	34.18
Telescope Magnification	10.5	10.5
Root Sum Square of TX and RX Deformation (μrad)	7.59	4.11
Budgeted Error (μrad)	5.396	5.396

4.3 Thermoelastic Model Summary

This Chapter discusses what thermoelastic modeling is and why it is important to model for the fine pointing budget of the mission. The development of the CLICK-B/C thermoelastic model is discussed and how the thermal model temperatures were used. The analysis performed in this section set an upper bound on the thermoelastic misalignment that will occur during operation of the CLICK-B/C payload. It is calculated that the thermal isolation of the optical bench from the EDFA plate, which it is mounted to, caused the optical plate to deform and misalign the optics by 10.84 μrad, which is double the 5.396 μrad budgeted allotted for this type of misalignment in the pointing budget. Two solutions were devised to mitigate the extent of the thermoelastic misalignment. The first, which was implemented in the analysis, is thermally coupling the optical plate to the EDFA plate to reduce the temperature difference between the two. The second is to redesign how the optical bench is mounted and add flexures to allow the optical bench and EDFA plate to have a large temperature difference without distorting the optical bench. It was calculated that the first option reduced the thermoelastic misalignment from 10.84 μrad to 4.82 μrad. The program will need to investigate the implications on the optical performance of the payload as the optics change temperature to ensure that this design choice is the best path forward to reduce thermoelastic misalignment.

Chapter 5

Conclusion

This chapter summarizes the analysis performed in the thesis, states contributions made throughout it, and proposes future work.

5.0.1 Thesis Summary

The work presented in this thesis supports the CLICK program development efforts by designing and characterizing the thermal control system of CLICK-A and CLICK-B/C as well as analyzing thermoelastic performance of the CLICK-B/C CubeSat laser communication payloads.

Chapter 1 introduces the CubeSat standard and discuses the current state of the art for CubeSat missions. Optical communication is introduced and its advantages and disadvantages of the technology are discussed. The CLICK mission, and its payloads are discussed.

Chapter 2 shows the approach to the thermal design of the CLICK payloads and important factors that went into the thermal design of each payload. A description of how the thermal control systems monitor and maintain the temperatures for each payload is discussed. The determination of the component temperature ratings is explained, as well as the TVAC testing that was performed on critical components to determine their space survivability and performance.

Chapter 3 discusses the development of the thermal model for both the CLICK-A

and -B/C payloads. The various inputs to the model are presented and the results of the model are reported. The CLICK-A components that did not use heaters all met the 10°C margin for their maximum and minimum operational temperature. The CLICK-A components with heaters were shown to preheat in 15 minutes and reach their minimum operational temperature. The CLICK-B/C components that did not use heaters almost all met the 10°C margin for their maximum and minimum operational temperature, but has motivated an increased in the interface temperature by 5°C between the spacecraft and payload for CLICK-B/C compared to CLICK-A. The CLICK-B/C components with heaters were shown to preheat in 10 minutes and reach their minimum operational temperature.

Chapter 4 discusses what thermoelastic modeling is and why it is important to model for the pointing budget of the mission. The development of the CLICK-B/C thermoelastic model is discussed and how the thermal model temperatures were used. The analysis performed in this section set an upper bound on the thermoelastic misalignment that will occur during operation of the CLICK-B/C payload. It is calculated that the thermal isolation of the optical bench from the EDFA plate, which it is mounted to, caused the optical plate to deform and misalign the optics by 10.84 μrad, which is double the 5.396 μrad budgeted allotted for this type of misalignment in the pointing budget. Two solutions were devised to mitigate the extent of the thermoelastic misalignment. The first, which was implemented in the analysis, is thermally coupling the optical plate to the EDFA plate to reduce the temperature difference between the two. The second is to redesign how the optical bench is mounted and add flexures to allow the optical bench and EDFA plate to have a large temperature difference without distorting the optical bench. It was calculated that the first option reduced the thermoelastic misalignment from 10.84 μrad to 4.82μrad.

5.0.2 Thesis Contributions

- Developed thermal control systems for the CLICK-A and CLICK-B/C payloads in Chapter 2

- Performed environmental testing on key components to determine survivability and performance in a simulated space environment in Section 2.1.2
- Developed thermal models for CLICK-A and CLICK-B/C payloads. Predicted temperatures of components to be within operational temperatures bounds during operation and preheating times for components that have heaters in Chapter 3
- Performed thermoelastic analysis of the CLICK-B/C optical bench to analyze the thermoelastic pointing errors induced during the transmission of the payload in Chapter 4

5.0.3 Future Work

- Assemble the CLICK-A payload and confirm the performance of the thermal control system.
- Perform thermal balance and performance environmental testing in a thermal vacuum chamber of the CLICK-A payload.
- Refine the maximum and minimum payload-to-bus interface temperatures for the CLICK-B/C payloads.
- Determine the optical performance impact of the predicted temperature range for the CLICK-B/C optical bench.
- Evaluate feasibility of the mounting the optical bench with flexures.
- Assemble the CLICK-B/C optical bench prototype and perform alignment of the optics.
- Assemble the CLICK-B/C engineering design unit and perform thermal balance and performance environmental testing in a thermal vacuum chamber.

Appendix A

Spacecraft Bus Interface Temperature Plots

Plots provided from the bus provider thermal engineer related to the worst case hot and cold models for each of the different faces that define in the payload-to-bus mechanical interface.

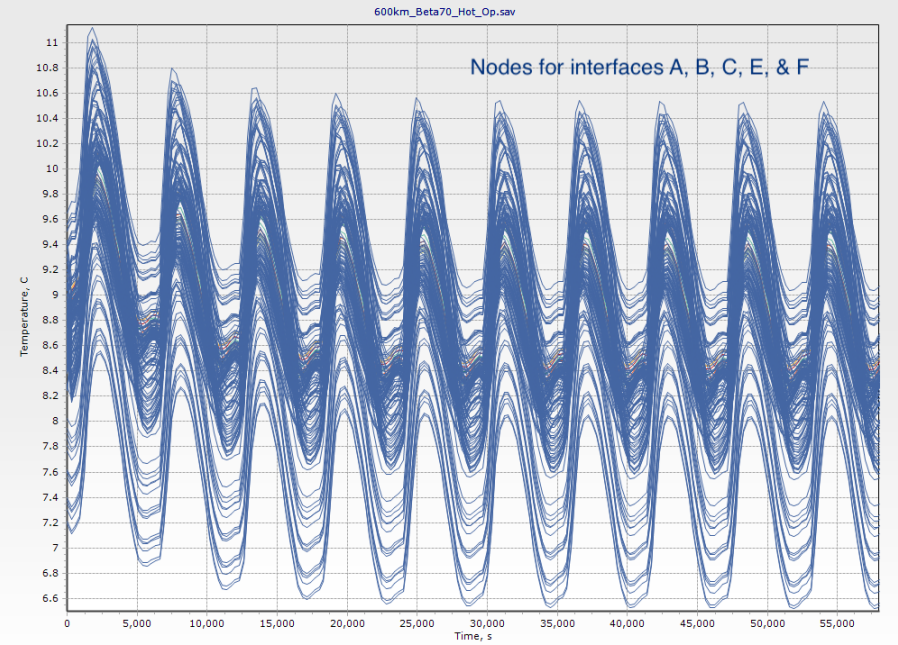

Figure A-1: Temperature of interface A,B,C,E, and F while the payload is not operating over multiple orbits for worst case hot.

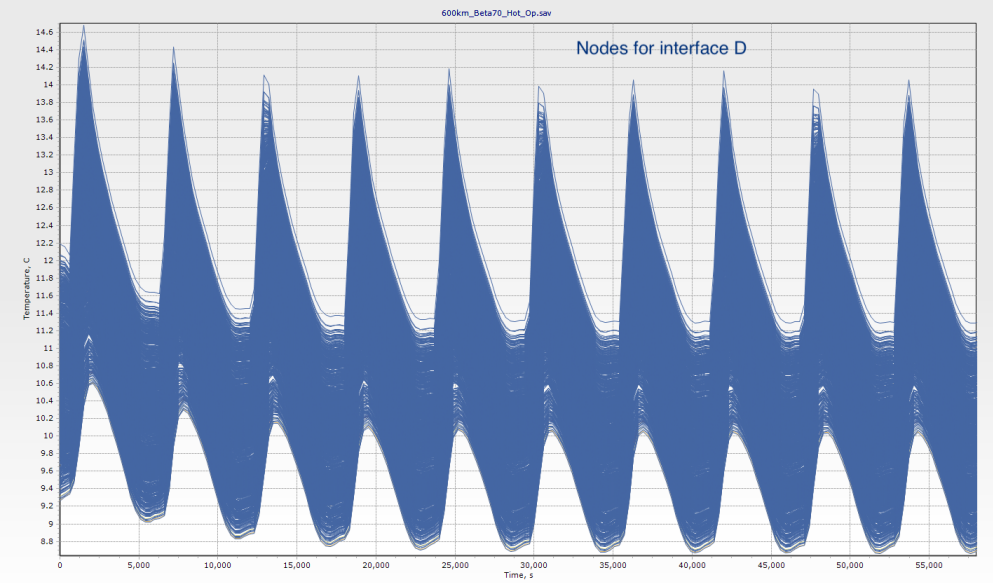

Figure A-2: Temperature of interface D while the payload is not operating over multiple orbits for worst case hot.

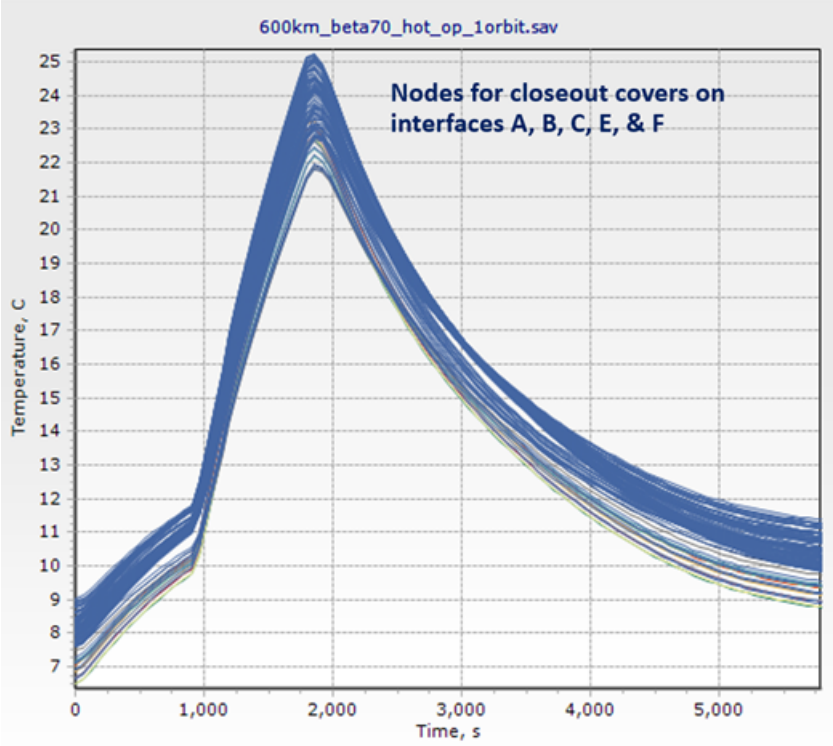

Figure A-3: Temperature of interface A,B,C,E, and F while the payload is operating over one orbit for worst case hot.

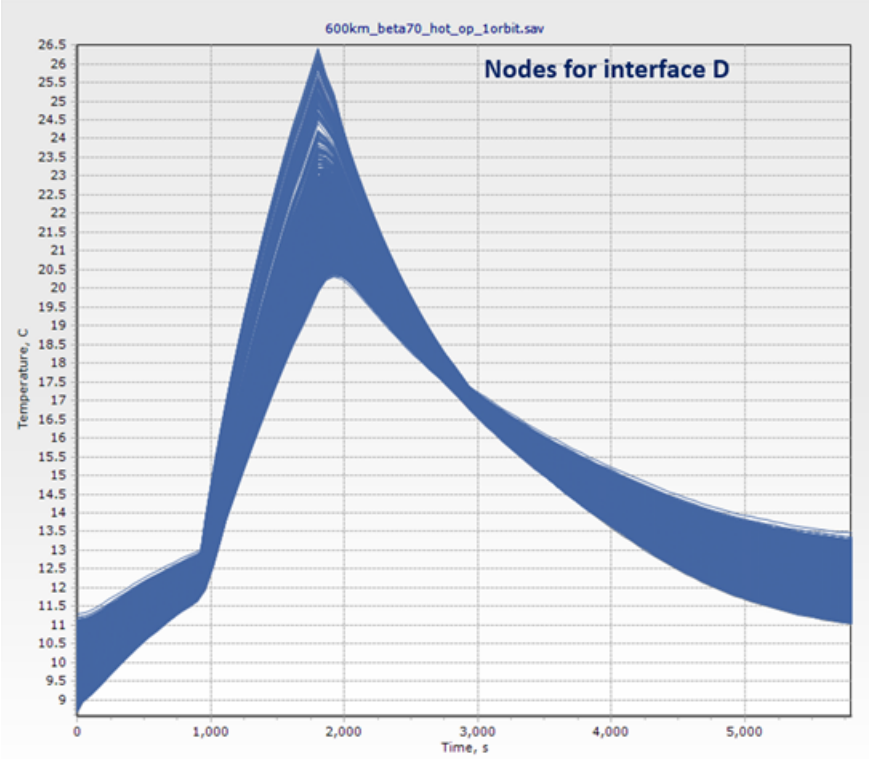

Figure A-4: Temperature of interface D while the payload is operating over one orbit for worst case hot.

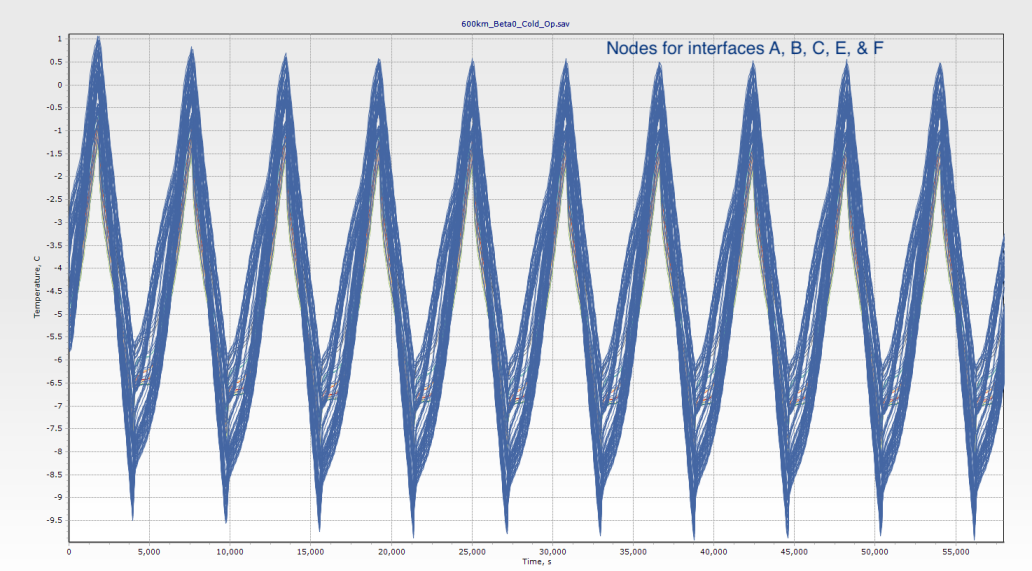

Figure A-5: Temperature of interface A,B,C,E, and F while the payload is not operating over multiple orbits for worst case cold.

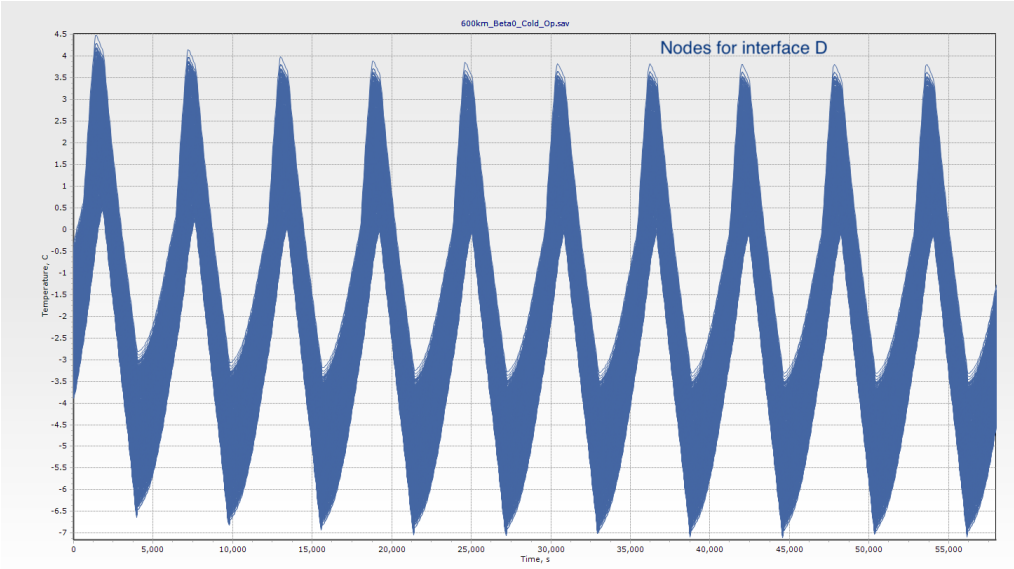

Figure A-6: Temperature of interface D while the payload is not operating over multiple orbits for worst case cold.

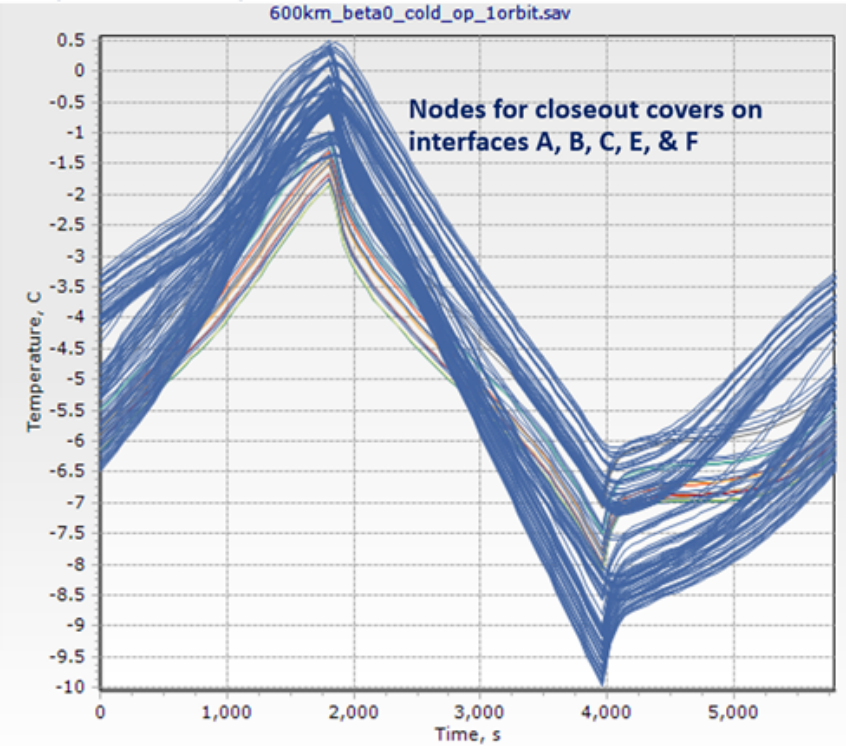

Figure A-7: Temperature of interface A,B,C,E, and F while the payload is operating over one orbit for worst case cold.

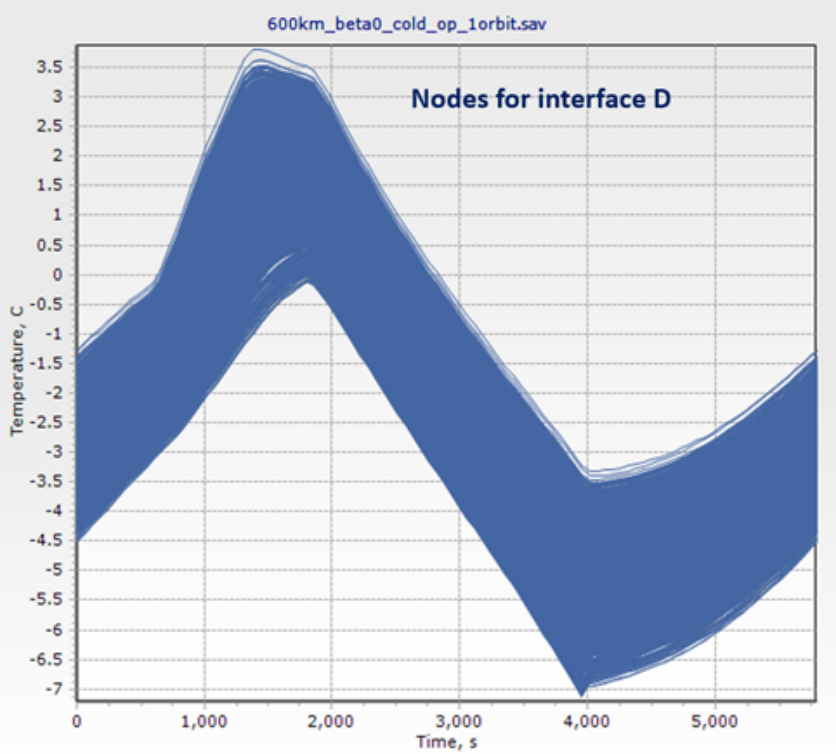

Figure A-8: Temperature of interface D while the payload is operating over one orbit for worst case cold.

Bibliography

[1] Martin N. Sweeting. Modern small satellites-changing the economics of space. *Proceedings of the IEEE*, 106:343–361, 3 2018. ISSN 15582256. doi: 10.1109/JPROC.2018.2806218.

[2] Robert Wright, Miguel Nunes, Paul Lucey, Luke Flynn, Sarath Gunapala, David Ting, Sir Rafol, Alexander Soibel, Chiara Ferrari-Wong, Andrea Gabrieli, and Prasad Thenabail. Hyti: thermal hyperspectral imaging from a cubesat platform. page 15. SPIE-Intl Soc Optical Eng, 8 2019. ISBN 9781510629554. doi: 10.1117/12.2530821.

[3] Kiruthika Devaraj, Matt Ligon, Eric Blossom, Joseph Breu, Bryan Klofas, Kyle Colton, and Ryan Kingsbury. Planet high speed radio: Crossing gbps from a 3u cubesat, 2019.

[4] Alberto Carrasco-Casado, Abhijit Biswas, Renny Fields, Brian Grefenstette, Fiona Harrison, Suzana Sburlan, and Morio Toyoshima. Optical communication on cubesats - enabling the next era in space science.

[5] Hank Heidt, Jordi Puig-Suari, Augustus S Moore, Shinichi Nakasuka, and Robert J Twiggs. Heidt ssc00-v-5 cubesat: A new generation of picosatellite for education and industry low-cost space experimentation, 2000.

[6] Cal Poly – San Luis Obispo. *CubeSat Design Specification.*

[7] Michael Swartwout. Cubesat database. URL `https://sites.google.com/a/slu.edu/swartwout/home/cubesat-database#refs`.

[8] Matthew W Smith, Amanda Donner, Mary Knapp, Christopher M Pong, Colin Smith, Jason Luu, Peter Di Pasquale, Robert L Bocchino, Brian Campuzano, Jessica Loveland, Cody Colley, Alessandra Babuscia, Mary White, Joel Krajewski, and Sara Seager. Ssc18-i-08 on-orbit results and lessons learned from the asteria space telescope mission, 2018.

[9] Andrew T Klesh, John Baker, and Joel Krajewski. Marco: Flight review and lessons learned.

[10] W. Blackwell, G. Allen, C. Galbraith, T. Hancock, R. Leslie, I. Osaretin, L. Retherford, M. Scarito, C. Semisch, M. Shields, M. Silver, D. Toher, K. Wight,

D. Miller, K. Cahoy, and N. Erickson. Nanosatellites for earth environmental monitoring: The micromas project. In *2012 12th Specialist Meeting on Microwave Radiometry and Remote Sensing of the Environment (MicroRad)*, pages 1–4, 2012.

[11] Steven Reising. Temporal experiment for storms and tropical systems technology demonstration (tempest-d) mission: Enabling time-resolved cloud and precipitation observations from 6u-class satellite constellations, 2020.

[12] Govind P. Agrawal. *Optical Communication: Its History and Recent Progress*, pages 177–199. Springer International Publishing, Cham, 2016. ISBN 978-3-319-31903-2.

[13] Hemani Kaushal and Georges Kaddoum. Free space optical communication: Challenges and mitigation techniques. 6 2015. URL `http://arxiv.org/abs/1506.04836`.

[14] F. J. Duarte. *Tunable laser optics*. CRC Press, 2017.

[15] Hamid Hemmati. *Near-Earth laser communications*. CRC Press, 2009.

[16] Kathleen Riesing. Development of a pointing, acquisition, and tracking system for a nanosatellite laser communications module. Master's thesis, 2015.

[17] T. S. Rose, D. W. Rowen, S. D. LaLumondiere, N. I. Werner, R. Linares, A. C. Faler, J. M. Wicker, C. M. Coffman, G. A. Maul, D. H. Chien, A. C. Utter, R. P. Welle, and S. W. Janson. Optical communications downlink from a low-earth orbiting 15u cubesat. *Optics Express*, 27:24382, 8 2019. ISSN 1094-4087. doi: 10.1364/oe.27.024382.

[18] Richard P Welle, Christopher M Coffman, Dee W Pack, and John R Santiago. Ssc19-iii-08 cubesat laser communication crosslink pointing demonstration, 2019.

[19] John Conklin. Ssc14-ix-05 optical time transfer for future disaggregated small satellite navigation systems, 2014.

[20] Ondrej Čierny and Kerri L. Cahoy. Click: Cubesat laser infrared crosslink. CubeSat Developers Workshop, 4 2019.

[21] Emily Clements, Raichelle Aniceto, Derek Barnes, David Caplan, James Clark, Iñigo del Portillo, Christian Haughwout, Maxim Khatsenko, Ryan Kingsbury, Myron Lee, Rachel Morgan, Jonathan Twichell, Kathleen Riesing, Hyosang Yoon, Caleb Ziegler, and Kerri Cahoy. Nanosatellite optical downlink experiment: design, simulation, and prototyping. *Optical Engineering*, 55:111610, 9 2016. ISSN 0091-3286. doi: 10.1117/1.oe.55.11.111610.

[22] Ryan W. Kingsbury. *Optical Communications for Small Satellites*. PhD thesis, Cambridge, MA, 2015.

[23] Ondrej Čierny and Kerri L. Cahoy. On-orbit beam pointing calibration for nanosatellite laser communications. *Optical Engineering*, 58:1, 11 2018. ISSN 1560-2303. doi: 10.1117/1.oe.58.4.041605.

[24] Kathleen Michelle Riesing. *Portable Optical Ground Stations for Satellite Communication*. PhD thesis, Cambridge, MA, 2018.

[25] Kerri Cahoy, Peter Grenfell, Angela Crews, Michael Long, Paul Serra, Anh Nguyen, Riley Fitzgerald, Christian Haughwout, Rodrigo Diez, Alexa Aguilar, John Conklin, Cadence Payne, Joseph Kusters, Chloe Sackier, Mia LaRocca, and Laura Yenchesky. The cubesat laser infrared crosslink mission (click). page 33. SPIE-Intl Soc Optical Eng, 7 2019. doi: 10.1117/12.2535953.

[26] Derek Barnes. Optomechanical design, analysis, and testing of the nanosatellite optical downlink experiment. Master's thesis, Cambridge, MA, 2018.

[27] David G. Gilmore and Martin Donabedian. *Spacecraft Thermal Control Handbook*. American Institute of Aeronautics and Astronautics, 2003.

[28] *Schneider Xenoplan 1.4/23 Datasheet*. Jos. Schneider Optische Werke GmbH, Ringstraße 132 55543 Bad Kreuznach, 10 2018.

[29] Solving problems with sinda/fluint. URL `https://spinoff.nasa.gov/spinoff2002/ct_9.html`.

[30] Sinda/fluint. URL `https://www.crtech.com/products/sindafluint`.

[31] URL `http://asm.matweb.com/search/SpecificMaterial.asp?bassnum=MA6061T6`.

[32] URL `http://www.matweb.com/search/DataSheet.aspx?MatGUID=61499d82439f466eba1689158032dbac`.

[33] James Paul Mason, Bret Lamprecht, Thomas N. Woods, and Chloe Downs. Cubesat on-orbit temperature comparison to thermal-balance-tuned-model predictions. *Journal of Thermophysics and Heat Transfer*, 32:237–255, 2018. ISSN 08878722. doi: 10.2514/1.T5169.

[34] M. M. Finckenor and R. F. Coker. *Optical Properties of Nanosatellite Hardware*. 2014.

[35] Lonny Kauder. *Spacecraft Thermal Control Coatings References*. 2005.

[36] Grant Gunnison. Click a conops - power modes spreadsheet. 11 2019.

[37] Keith B. Doyle, Victor L. Genberg, and Gregory J. Michels. *Integrated optomechanical analysis*. SPIE Press, 2012.

[38] Peter Grenfell. Design and prototyping of a nanosatellite laser communications terminal for the cubesat laser infrared crosslink (click) b/c mission. Small Satellite Conference, 2020.

[39] Ondrej Čierny. Testing of the cubesat laser infrared crosslink (click-a) payload. Small Satellite Conference, 2020.

[40] Michael J. Long. Pointing acquisition and tracking design and analysis for cubesat laser communication crosslinks. Master's thesis, Cambridge, MA, 2018.

[41] Laura Yenchesky. Optomechanical design for cubesat laser infrared crosslinks. Master's thesis, Cambridge, MA, 2019.

[42] Gerald E. Farin and Dianne Hansford. *Practical linear algebra: a geometry toolbox*. CRC Press, Taylor Francis, 2014.

[43] Eric W Weisstein. Dihedral angle. URL `https://mathworld.wolfram.com/DihedralAngle.html`.